GDCh

**Research Articles**

*Angewandte* *Chemie*
International Edition
www.angewandte.org

Check for updates

**Nanosheets** Hot Paper

# Photo-Controlled Gating of Selective Bacterial Membrane Interaction and Enhanced Antibacterial Activity for Wound Healing

*Jagabandhu Sahoo, Soumyashree Sahoo, Yogeswari Subramaniam, Preeti Bhatt, Subinoy Rana,\* and Mrinmoy De\**

**Abstract:** Reversible biointerfaces are essential for on-demand molecular recognition to regulate stimuli-responsive bioactivity such as specific interactions with cell membranes. The reversibility on a single platform allows the smart material to kill pathogens or attach/detach cells. Herein, we introduce a 2D-MoS$_2$ functionalized with cationic azobenzene that interacts selectively with either Gram-positive or Gram-negative bacteria in a light-gated fashion. The *trans* conformation (***trans*-Azo-MoS$_2$**) selectively kills Gram-negative bacteria, whereas the *cis* form (***cis*-Azo-MoS$_2$**), under UV light, exhibits antibacterial activity against Gram-positive strains. The mechanistic investigation indicates that the ***cis*-Azo-MoS$_2$** exhibits higher affinity towards the membrane of Gram-positive bacteria compared to ***trans*-Azo-MoS$_2$**. In case of Gram-negative bacteria, ***trans*-Azo-MoS$_2$** internalizes more efficiently than ***cis*-Azo-MoS$_2$** and generates intracellular ROS to kill the bacteria. While the ***trans*-Azo-MoS$_2$** exhibits strong electrostatic interactions and internalizes faster into Gram-negative bacterial cells, ***cis*-Azo-MoS$_2$** primarily interacts with Gram-positive bacteria through hydrophobic and H-bonding interactions. The difference in molecular mechanism leads to photo-controlled Gram-selectivity and enhanced antibacterial activity. We found strain-specific and high bactericidal activity (minimal bactericidal concentration, 0.65 μg/ml) with low cytotoxicity, which we extended to wound healing applications. This methodology provides a single platform for efficiently switching between conformers to reversibly control the strain-selective bactericidal activity regulated by light.

## Introduction

Dynamic control of the cell-material interface is of great interest for fundamental research as well as practical applications such as tissue engineering, drug delivery, bio-interfacing and cell-based diagnostics.[1–4] The dynamic control allows capture/release of cancer cells, controlled cell adhesion, and killing/release of bacteria using external stimuli.[5–7] Numerous stimuli-responsive bio-interfaces have been developed which are controlled by various stimuli, including pH,[8–10] temperature,[11–12] enzymes,[13–15] electric potential,[16–17] and light.[6,18–19] Among them, a light-responsive system offers the benefits of precise spatiotemporal control, non-invasive and convenient operation, making it appropriate for biomedical applications without impacting the normal biological processes.[20–22]

Azobenzene provides an ideal photoswitchable candidate for regulating the interaction between material and biointerface.[23] The reversible photoisomerization between *cis* and *trans* conformations can be regulated by adjusting the irradiation's wavelength.[24–25] Recently, azobenzene-functionalized materials have been widely utilized to construct the photo-switchable bio-interfaces[26] including reversible cell adhesion,[27] immobilization of bacteria[28] and proteins.[29–30] For example, Liu et al. reported self-assembled monolayers to obtain a surface with reversible control of cell adhesion on a molecularly well-defined surface.[27] Depending on the conformation of azobenzene, this surface can either permit or prevent cell attachment. The reversibility between two states can be regulated by different wavelengths of light. However, similar strategy hasn't been employed so far to dynamically modulate the interaction between bacterial membrane and azobenzene embedded surface. Wei et al. created a biointerface that can kill and concurrently release dead bacteria under the influence of UV/Visible light.[31] Yang et. al constructed a hydrophilic polymeric brush with cyclodextrin (CD)-modified antifouling polymer incorporated with azobenzene (**Azo**). When exposed to UV light, the azo- based bactericidal polymer is released together with the dead bacteria.

A growing threat to the public health is posed by microbial infection brought on by pathogens. For the treatment, a wide range of functionalized nanomaterial-based antibiotics including carbon-based materials,[32–33] zwitterionic polymers,[34–35] metals/metal oxide nanomaterials,[36–38] cationic polymeric nanomaterials have been developed recently.[39] The broad spectrum of antibacterial drugs have

[*] J. Sahoo, S. Sahoo, Prof. M. De
Department of Organic Chemistry, Indian Institute of Science
Bengaluru 560012 (India)
E-mail: md@iisc.ac.in

Y. Subramaniam
Department of Biochemistry, Indian Institute of Science
Bengaluru 560012 (India)

P. Bhatt, Dr. S. Rana
Materials Research Centre, Indian Institute of Science
Bengaluru 560012 (India)
E-mail: subinoy@iisc.ac.in

demonstrated remarkable effect against multi-bacterial infections, but the long term use damage the balance of microbial flora at the site of infection. This may lead to greater resistance, which would then limit their therapeutic efficacy.[40–41] Several cationic antimicrobials have been developed to specifically target the negative surface membrane of bacteria.[42–45] Most of the cationic antimicrobials have shown excellent activity against multi-drug-resistant strains but failed to show any selectivity. The evolution of drug resistance and the negative effects brought on by general bactericidal action can both be slowed down by the development of selective antimicrobials.[46–52] By manipulating the surface charge on self-assembled monolayers of gold nanoparticles, Grzybowski and colleagues have achieved the Gram-selectivity.[53] More recently from our group, we have reported Gram-selective antibacterial agent by tuning the surface charge on 2D-MoS$_2$.[54] The equilibrium of polyvalent, and non-covalent interactions with the bacterial membrane can be endowed with the selectivity achieved by surface charge regulation. But in all such reports either by us or other research groups created the selective antibacterial agents with selective functionalization or by stimuli-responsive releases. Due to irreversibility of such system, it is difficult to tune the bactericidal activity and eradicate the infections caused by mixed strains. However, the reversible and selective antibacterial activity has not achieved yet. Therefore, it is highly desirable to establish photo-switchable selective bactericidal agents.

In this work, we have developed a photoswitchable selective antibacterial agent based on **Azo**-functionalized 2D-MoS$_2$ with cationic headgroup. We have considered 2D-MoS$_2$, as it shows inherent antibacterial property which can be enhanced with surface functionalization.[36–37,55–56] As shown in Scheme 1, the UV and visible light irradiation switches between the *cis* and *trans* conformation (hereafter known as ***cis*-Azo-MoS$_2$** and ***trans*-Azo-MoS$_2$**, respectively)
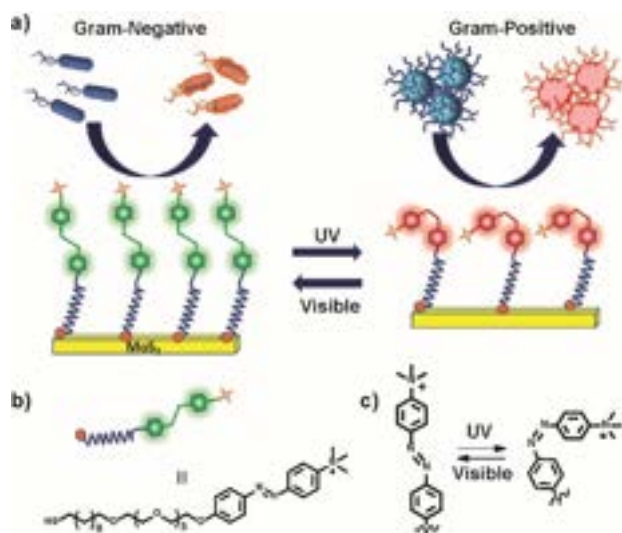
of the smartly designed ligand. Consequently, the cationic quaternary ammonium headgroups are exposed outward in case of ***trans*-Azo-MoS$_2$**, with a buried cationic group for the *cis* conformer. While both the conformations showed excellent bactericidal activity (minimum bactericidal concentration, MBC, as low as 0.65 µg/mL), they exhibited differential light-gated sensitivity against Gram-positive methicillin-resistant *Staphylococcus aureus* (MRSA) and Gram-negative *Pseudomonas aeruginosa* (*P. aeruginosa*) bacterial strains. Detailed analysis of the molecular mechanism of bactericidal activity revealed an intriguing **Azo** isomer-dependent bacterial membrane interaction, which stems from the inherent difference in the membrane composition of the bacterial strains. Compared to the monofunctionalized ligands or mixed monolayer for achieving Gram-selectivity discussed above, this fully reversible material enables selectivity under different light conditions. Notably, the same platform can be used to eradicate both types of bacterial strains, including multi-drug resistant ones, by a "on-off" light irradiation cycle. Given the efficacy and biocompatibility of the stimuli-responsive antibacterial **Azo-MoS$_2$**, we evaluated wound healing efficiency using a mouse model of an infected lesion with MRSA. Compared to ***trans*-Azo-MoS$_2$** and conventional antibiotic (e.g., vancomycin) treatments, our experimental findings demonstrate that ***cis*-Azo-MoS$_2$** based therapy was very effective and resulted faster wound healing against MRSA infection. In all, we demonstrate a light stimulus-responsive nanomedicine that features bacteria selectivity and enhanced killing efficiency, establishing the molecular mechanism of interactions.

## Results and Discussion

### Functionalization of exfoliated 2D-MoS$_2$

Single layered 2D-MoS$_2$ was chemically exfoliated from the bulk MoS$_2$ by lithium intercalation method.[57] The formation of single layer 2D-MoS$_2$ was confirmed by atomic force microscopy (AFM) analysis and transmission electron microscope (TEM) imaging (Figure S4).

The photo switchable thiolated azo ligand (**Azo-SH**) was designed to meet certain criteria. For instance, the ligand has an alkyl chain to enhance the stability of 2D-MoS$_2$ surface, a thiol to anchor chemically exfoliated MoS$_2$ (ce-MoS$_2$) at one end, and tetraethylene glycol (TEG) for biocompatibility and water solubility. Besides, the azo-containing head group would impart photo-switching in presence of light of two different wavelengths. The terminal end of the head group comprises of the quaternary ammonium group to interact effectively with the negative bacterial membrane (Scheme 1). The ligand was synthesized in good yield and details are summarized in the Supporting Information (Figure S1, S2, S3). Finally, ce-MoS$_2$ was functionalized with the photo-switchable thiol ligands using an established method developed in our lab.[58]

Zeta potential measurements were used to validate conjugation of ce-MoS$_2$. The efficient functionalization of 2D-MoS$_2$ is demonstrated by the increase in the zeta



**Scheme 1.** (a) Schematic representation of selective antibacterial activity of photoswitchable **Azo-MoS$_2$**. (b) The cationic azo ligand with a thiol end. (c) The photoswitching activity of azo group.

potential value of ce-MoS$_2$ from $-47.1$ to $+44.3$ mV (Figure 1a). The observed zeta potential for **trans-Azo-MoS$_2$** is $+44.3$ mV, whereas the value for **cis-Azo-MoS$_2$** is $+36.8$ mV. The cationic head group is expected to be exposed in case of the **trans** functionalized MoS$_2$. However, the ligand headgroup should be buried inside for the **cis** functionalization, leading to a larger positive surface zeta potential value for **trans-Azo-MoS$_2$** than **cis-Azo-MoS$_2$**. The anchoring of ligand to ce-MoS$_2$ was further confirmed from IR spectra (Figure 1b). The peaks between 2917 cm$^{-1}$ and 2849 cm$^{-1}$corresponds to the asymmetric stretching vibrations of $-CH_3$ and $-CH_2-$ which is observed after functionalization with 2D-MoS$_2$. The band due to $-N=N-$ bond vibration of **Azo** ligand at 1500 cm$^{-1}$ before and after functionalization is also significant to confirm the functionalization of ligand. The C–N stretching occurs at 1230 cm$^{-1}$ after functionalization proves the conjugation of ligand.

### Photoswitching of functionalized MoS$_2$

The photoswitching of the ligand alone and of the ligand functionalized 2D-MoS$_2$ was studied by using ultraviolet-visible (UV/Vis) spectrophotometry. From Figure 1c, we can see that the peak at 350 nm from **trans** disappears upon 120 s irradiation of UV light (365 nm) which is due to the formation of **cis** conformation. After 120 s of visible light irradiation, the same peak reappears, confirming the **cis-trans** isomerization using UV/Vis light irradiation. Following

functionalization of this ligand on the surface of 2D-MoS$_2$, similar isomerization was observed. From Figure 1d, we can see that irradiation with the UV light (365 nm) led to disappearence of the peak corresponding to the **trans-Azo-MoS$_2$**. The peak reappears after the irradiation with visible light. We have also quantified the percentage of conversion in response to UV light. It was calculated by considering the absorbance value of **Azo-MoS$_2$** before and after irradiation of UV light. The data shows that the solution contain total 60 % **cis** form after 2 min irradiation with UV light. Not only by irradiation with different wavelength, the **cis-trans** switching was also observed at 37 °C. From the Figure S5, we can see that **cis** converts to **trans** with time at 37 °C. For reference, the peak corresponds to **trans** and **cis-Azo-MoS$_2$** are also given. It can be clearly observed that the **cis** conformation transforms to **trans** after 1 hr. Due to this temperature dependent switching of the **Azo** ligand, all the antibacterial activity experiments were carried out at room temperature (25 °C). It was observed that light dependent switching is comparatively faster than the temperature dependent process. Further, we tested the stability of **cis** conformation after irradiation under UV light. The auto switching of **cis** to **trans** in dark was established by measuring UV-Vis spectra at different time intervals (Figure 1e). The conversion was not observed upto 24 h which shows excellent stability of the **cis** conformation under the dark condition. Then, we performed **cis-trans** transition cycles by using UV/Vis irradiation at 365 nm (Figure 1f). The multiple cycle of **cis-trans** transition confirms the
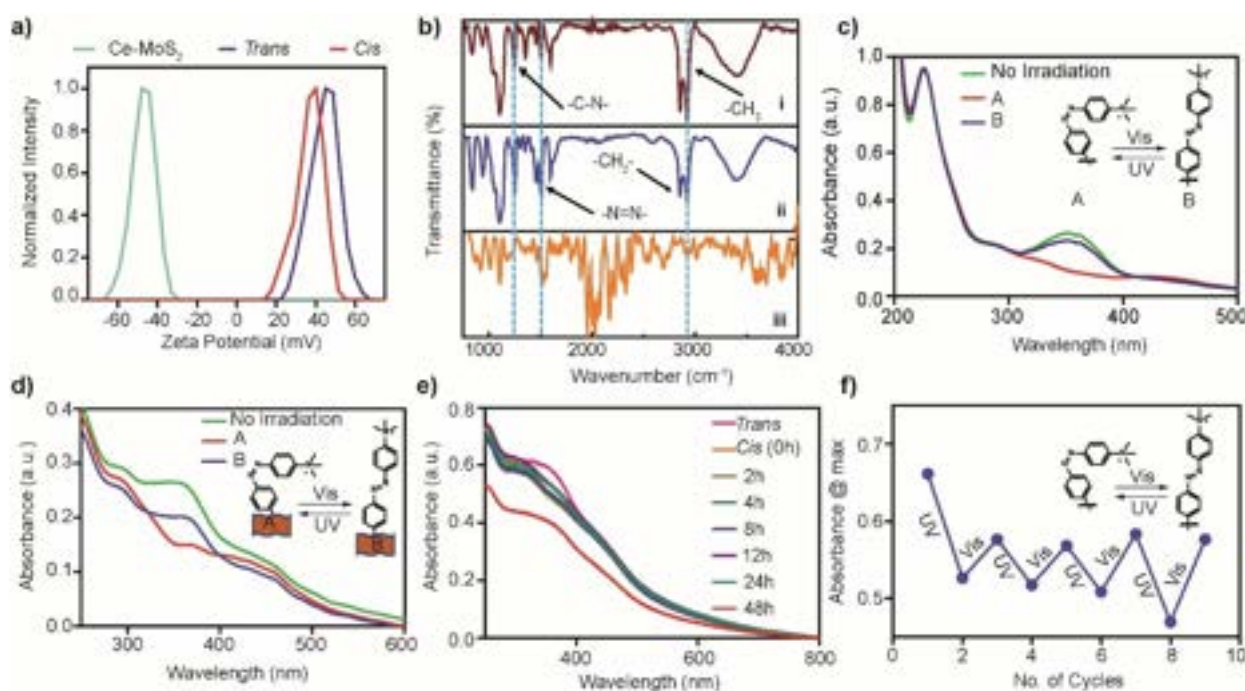


**Figure 1.** The characterization and photoswitching activity of functionalized 2D-MoS$_2$. (a) Zeta potential measurement for chemically exfoliated (ce-MoS$_2$: $-47.1$ mV) and **cis** ($+36.8$ mV) and **trans-Azo-MoS$_2$** ($+44.3$ mV). (b) Infrared (IR) spectra of (i) **Azo-SH**, (ii) **Azo-MoS$_2$**, (iii) ce-MoS$_2$. (c) The photo-switching behaviour of **Azo-SH** under irradiation of ultraviolet (UV $\approx$ 365 nm) and Visible (Vis) light. (d) The **cis-trans** photoswitching behaviour of **Azo-MoS$_2$**. (e) The stability of **cis-Azo-MoS$_2$** at room temperature after UV irradiation. (f) The cycle of **cis-trans** switching after on-off UV/Vis irradiation at 365 nm.

stability of functionalized $MoS_2$ after repeated exposure to UV/Vis light.

### Antibacterial activity of functionalized $MoS_2$

The antibacterial activity of functionalized $2D$-$MoS_2$ was assessed after estimating the photo switching behaviour of **Azo-MoS₂**. We have considered two different bacterial strains, Gram-positive methicillin resistant MRSA and Gram-negative *P. aeruginosa* as two representatives of ESKAPE pathogens.[59] The MBC values were determined with different concentration of functionalized $2D$-$MoS_2$ (Figure 2). It can be observed from Figure 2(c,d) that **cis-Azo-MoS₂** has superior bactericidal activity to **trans-Azo-MoS₂** against MRSA, with an MBC value of 0.65 µg/mL. With a similar MBC value (0.65 µg/mL), **trans-Azo-MoS₂** is more effective against *P. aeruginosa* bacteria than the **cis-Azo-MoS₂**.

We performed fluorescence microscopy and morphological analyses of bacteria using TEM to further support the aforementioned findings. By using confocal microscopy, live and dead bacterial cells were distinguished using fluorescent labelling. The propidium iodide (PI) generally stains the damaged cell membrane of dead bacteria while calcein-AM stains live cells. From the Figure 3a, MRSA that has been treated with **cis-Azo-MoS₂** does not exhibit green fluorescence. However, in the case of **trans-Azo-MoS₂** treated MRSA, the bacteria displayed both green and red fluorescence, indicating the presence of more living cells. This result is consistent with the observed antibacterial activity against MRSA.

The bactericidal activity of **Azo-MoS₂** was also supported by the study of treated bacteria using TEM. The altered membrane morphologies of the treated bacteria were captured. For untreated MRSA, the image in Figure 3b(i) depicts the correct bacterial morphology and membrane integrity. The **cis-Azo-MoS₂** treated MRSA has a more distorted shape and compromised membrane than the **trans-Azo-MoS₂** treated bacteria, as observed in Figure 3b-(ii,iii). Similarly, untreated *P. aeruginosa* demonstrate no membrane damage (Figure 3b(iv)), while bacteria treated
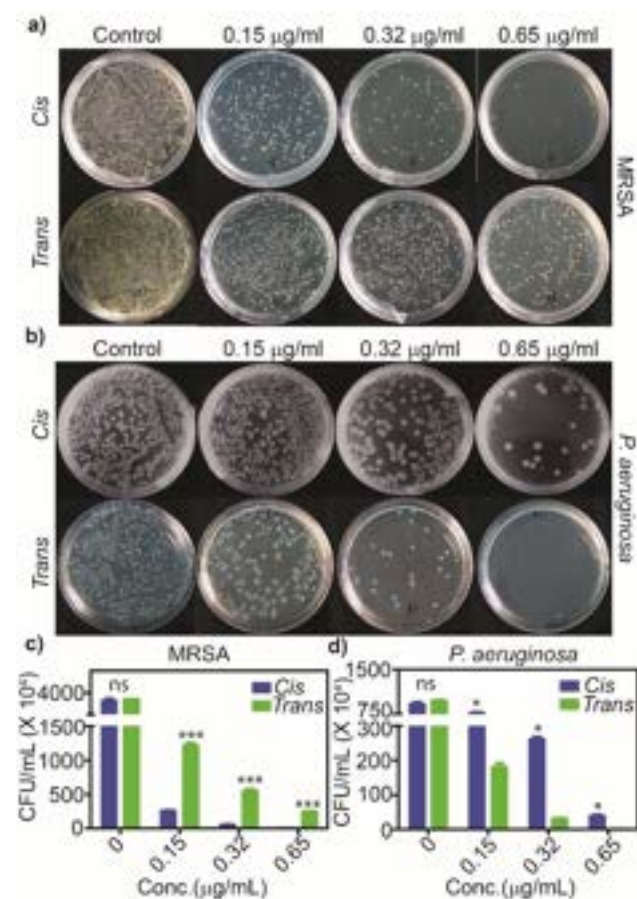
**Figure 2.** The bactericidal activity of bacteria after treated with different concentrations of *cis* and **trans-Azo-MoS₂**. (a, c) against MRSA ***p < 0.0001 and (b,d) *P. aeruginosa* *p < 0.01 by using colony forming unit (CFU) method (N = 3), ns—not significant.
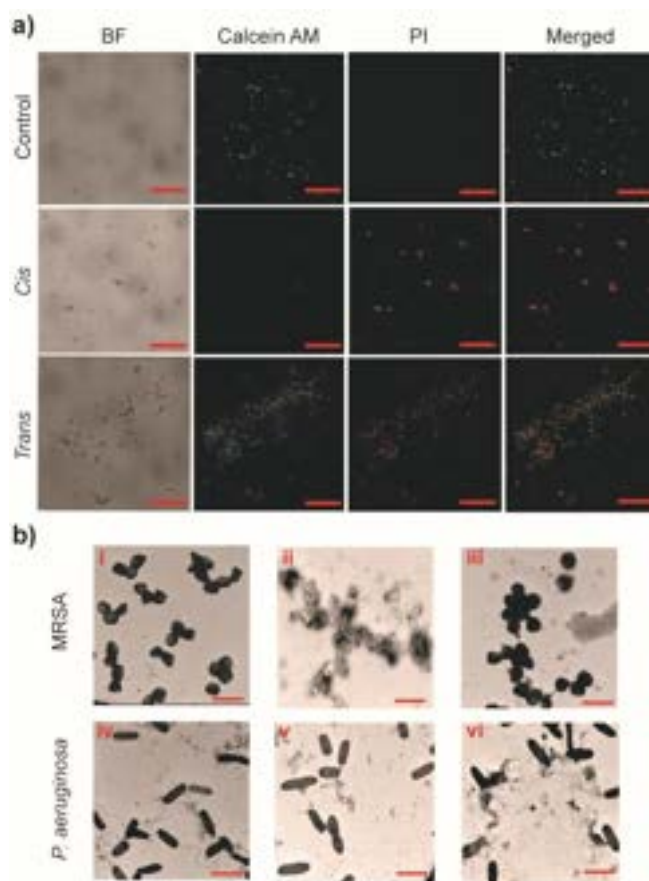
**Figure 3.** (a) Live-dead assay for MRSA using Calcein-AM and propidium iodide (PI) after treating with 10×MBC of *cis* and **trans-Azo-MoS₂** (Scale bar: 10 mm). The confocal imaging was performed with an excitation 488 nm and emission 520 nm for calcein-AM and excitation of 580 nm and an emission of 620 nm for PI. (b) Morphological analysis for MRSA bacteria using TEM of (i) Control, and after treated with 10×MBC (ii) **cis-Azo-MoS₂**, (iii) **trans-Azo-MoS₂** and *P. aeruginosa* (iv) Control, and after treated with 10×MBC of (v) **cis-Azo-MoS₂**, (vi) **trans-Azo-MoS₂**. (Scale bar: 1 mm).

with *cis*-**Azo-MoS₂** do not affect their morphology (Figure 3b(v)). However, the bacteria treated with *trans*-**Azo-MoS₂** exhibited substantial membrane damage and the leakage of internal fluids (Figure 3b(vi)). This further strengthens the selectivity in bactericidal activity.

Futhermore, the bactericidal activity and selectivity was examined for the free ligand (**Azo-SH**). As shown in Figure S6, similar phenomena was observed where *cis* conformation showed higher bactericidal activity against MRSA bacteria than *trans*. However, the bactericidal concentration is comparatively high (500 µg/mL). Incorporation of the ligand onto MoS₂ significantly improved the MBC value to 0.65 µg/mL. In general, surface charge of pristine exfoliated MoS₂ without any surface functionalization presents negatively chraged surface that interacts weakly with negatively charged bacterial membrane leading to high MBC value. However, the cationic ligand functionalization helps MoS₂ strongly bind the bacterial membrane and cause efficient antibacterial activity. This results indicates that the functionalization of photoswitching cationic ligand with 2D-MoS₂ has synergistically enhanced antibacterial activity. In addition, we have also compared the bactericidal activity of *cis*-**Azo-MoS₂** against both resistant and non-resistant bacteria. The *S. aureus* (SA) bacateria as a representative of non-resistant bacteria and MRSA as a representative of resistant bacteria were tested. As shown in Figure S7, the bcatericidal concncetration is low for SA bacteria (0.1 µg/mL) compared to MRSA (0.65 µg/mL). For drug-resistant bacteria, the bactericidal concentration is very high compared to non-resistant bacteria which is obvious. These results indicate that the Gram-selective antibacterial activity is due to only ligand and the material has shown higher bactericidal activity against non-resistant bacteria. It is also known that nanomaterials have less possibility of developing drug resistance.[60]

### Mechanistic investigation of selective antibacterial activity

Earlier studies reported the antibacterial activity of functionalized 2D-MoS₂ mainly depends on the generation of oxidative stress and effect on bacterial membrane.[36] As the core of the 2D-MoS₂ is same in both cases, the generation of oxidative stress is expected to be same. Therefore, membrane interaction and its impact on membrane permeability may be the source of any potential selectivity.

By monitoring the uptake of propidium iodide (PI) dye, the outer membrane permeabilization assay was carried out to demonstrate the selectivity. The PI uptake increases with the increasing damage of bacterial membrane. Figure 4(a,b) shows that the *cis*-**Azo-MoS₂** damages the bacterial membrane of MRSA more than the *trans*-**Azo-MoS₂**, which leads to more PI absorption. *Trans*-**Azo-MoS₂** resulted higher PI uptake in the case of *P. aeruginosa* than *cis*-**Azo-MoS₂**, suggesting that *trans* is more effective in damaging the *P. aeruginosa* bacterial membrane than *cis*. This data suggests that the selectivity was mostly resulting from the interaction between the bacterial membrane and different conformations of **Azo-MoS₂**.
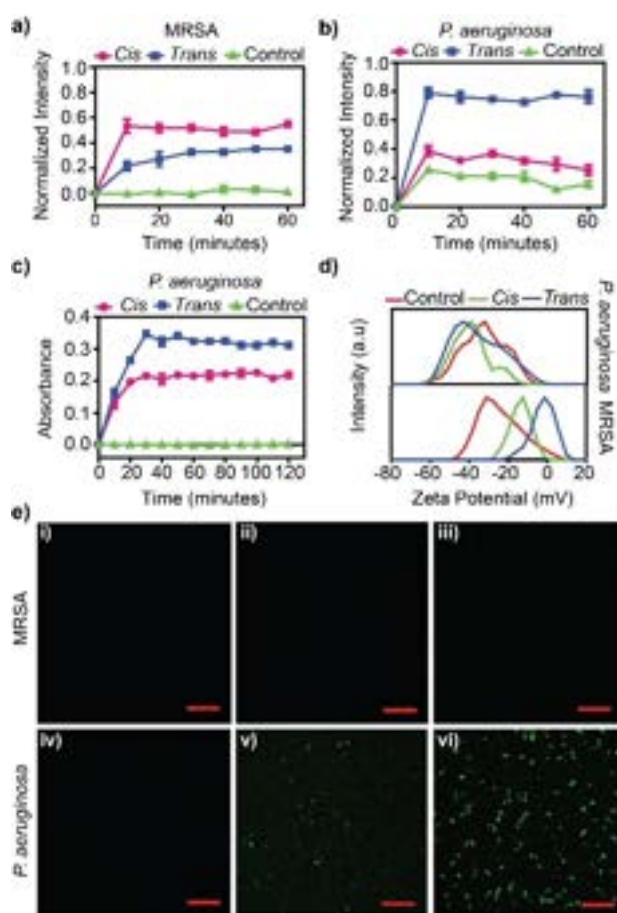


**Figure 4.** Mechanistic investigation of selective antibacterial activity. Outer Membrane permeabilization assay with propidium iodide after treated with 10×MBC of *cis* and *trans*-**Azo-MoS₂** (a) MRSA, (b) *P. aeruginosa*. The fluorescence was monitored with an excitation wavelength of 580 nm and an emission wavelength of 620 nm. (c) Inner membrane permeabilization assay with ortho-nitrophenyl-β-galactoside (ONPG, 10 mg/mL) against *P. aeruginosa* after treated with 10×MBC of *cis* and *trans*-**Azo-MoS₂**. The absorbance was measured at 420 nm. (d) Zeta potential measurement of MRSA and *P. aeruginosa* bacteria treated with *cis* and *trans*-**Azo-MoS₂** (10×MBC). (e) Determination of intracellular ROS generation using DCFDA assay. MRSA bacteria after treated with (i) Control, (ii) *cis*-**Azo-MoS₂**, (iii) *trans*-**Azo-MoS₂**. *P. aeruginosa* bacteria after treated with (iv) Control, (v) *cis*-**Azo-MoS₂**, (vi) *trans*-**Azo-MoS₂** (10×MBC).

We have also investigated the effect on the inner membrane of bacteria which is present only in Gram-negative bacteria. We used ortho-nitrophenyl-β-galactoside (ONPG), as an outer membrane permeable substrate, which cannot penetrate the inner membrane of Gram-negative bacteria such as *P. aeruginosa*. ONPG is also a chromogenic substrate for β-galactosidase (β-gal). The inner membrane disruption can leak cytoplasmic β-gal and reacts with ONPG to produce ortho-nitrophenol, which can be monitored by absorbance at 420 nm. To investigate whether *cis* and *trans*-**Azo-MoS₂** damage the permeabilization of the inner membrane of *P. aeruginosa*, ONPG was added to the treated bacterial suspension. Figure 4c shows that *trans*-**Azo-MoS₂** is more effectively disrupts the inner membrane of *P.*

*aeruginosa* than *cis*-Azo-MoS$_2$. This can be correlated with the high antibacterial activity of *trans*-Azo-MoS$_2$ against *P. aeruginosa*.

To probe the effect of different conformation on membrane depolarization, we performed the membrane depolarization assay by considering both MRSA and *P. aeruginosa* bacteria. The membrane depolarization was studied by using 3,3′-dipropylthiadicarbocyanine iodide (DISC3(5)) fluorescent probe.[61] This cationic dye accumulates in the confined interior of the bacterial membrane, as the bacterial membrane is composed of negatively charged components such as lipids and teichoic acids. The accumulation of dye usually results self-quenching of fluorescence. Any material that depolarizes the surface charge of the membrane causing release of dye which can be estimated by measuring fluorescence. Figure S9(a) indicates that *cis*-Azo-MoS$_2$ with higher hydrophobicity and less cationic charge exhibited high membrane depolarization against MRSA bacteria than *trans*-Azo-MoS$_2$. In contrast, the *trans*-Azo-MoS$_2$ with higher positive charge had shown higher membrane depolarization against *P. aeruginosa* than *cis*-Azo-MoS$_2$ as shown in Figure S9(b). This result indicates that the different conformation of **Azo-MoS$_2$** selectively depolarizes the bacterial membrane of Gram-positive and Gram-negative bacteria.

Furthermore, it is important to study the contribution of other factors such as reactive oxygen species (ROS) generation in selective antibacterial activity. Due to its inherent optoelectronic properties, 2D-MoS$_2$ is well known for its ability to generate ROS.[62] Hence, ROS generation by the functionalized 2D-MoS$_2$ was estimated by Ellman's assay. The abiotic oxidative stress was quantified by using 10×MBC concentrations of both the functionalized 2D-MoS$_2$. **Figure S10** shows that the two distinct conformations of **Azo-MoS$_2$** do not significantly differ in terms of ROS production, validating the generation of ROS is not impacted by the ligand conformations, rather the common 2D-MoS$_2$ core. This assay demonstrates that selective killing of Gram-positive and Gram-negative bacteria is not caused by extracellular ROS production rather it helps to reduce the concentration of dosage.

We continued to investigate the effect of *cis* and *trans*-Azo-MoS$_2$ interaction on the surfaces of Gram-positive (MRSA) and Gram-negative (*P. aeruginosa*) bacterial membrane by measuring their zeta potential. Both the bacterial strains feature highly negative surface charge as shown in Figure 4d. MRSA bound to *cis*-Azo-MoS$_2$, changed the membrane potential from −31.3 mV to −12.5 mV, whereas *trans*-Azo-MoS$_2$ caused the membrane potential reduced to −1.33 mV (Figure 4d). While *trans*-Azo-MoS$_2$ exhibited a greater shift towards positive potential due to the exposed cationic head group, it showed lesser bactericidal effect against MRSA bacteria than *cis*-Azo-MoS$_2$. This suggests that non-covalent interactions other than electrostatics are responsible for high antibacterial activity of *cis*-Azo-MoS$_2$ against MRSA. But when *cis* and *trans*-Azo-MoS$_2$ were treated against *P. aeruginosa* bacteria, it was found that *P. aeruginosa* surface potential cannot be reduced by either *cis* or *trans*-Azo-MoS$_2$ (Figure 4d). This

data indicates that only electrostatic interaction is not sufficient to alter the charge on Gram-negative bacteria which could be due to presence of both outer and inner membrane. Therefore, it is necessary to find out the possibility of internalization of *cis* or *trans*-Azo-MoS$_2$ followed by intracellular ROS generation to prove the effectiveness of *trans*-Azo-MoS$_2$ over *cis*-Azo-MoS$_2$.

We evaluated intracellular ROS generation to demonstrate the internalization of *cis* and *trans*-Azo-MoS$_2$ into MRSA and *P. aeruginosa*. The level of intracellular ROS generation was assessed using the fluorescent probe 2′,7′-dichlorofluorescin diacetate (DCFDA). When exposed to ROS species like the hydroxyl and peroxyl radicals, the DCFDA internalises into cells and undergoes deacylation, transforming into the green fluorescent compound 2′,7′-dichlorofluorescein (DCF). Bacteria were imaged using confocal microscopy after being treated with *cis*- and *trans*-Azo-MoS$_2$. Imaging showed that there was no intracellular ROS generation in the case of MRSA, demonstrating that neither of the functionalized MoS$_2$ was internalised (Figure 4e(iii)). However, *P. aeruginosa* showed substantial intracellular ROS generation with *trans*-Azo-MoS$_2$, (Figure 4e(vi)) but fewer cells were fluorescent with *cis*-Azo-MoS$_2$ treatment (Figure 4e(v)). From this data, it can be concluded that *trans*-Azo-MoS$_2$ binds with the membrane of Gram-negative bacteria more effectively than *cis*-Azo-MoS$_2$. Consequently, the internalization followed by intracellular ROS generation is more for *trans*-Azo-MoS$_2$ than the *cis* isomer. However, the intracellular ROS generation was not observed in Gram-positive bacteria by niether of the materials. This observation implies that both *cis*- and *trans*-Azo-MoS$_2$ depolarize the bacterial membrane of Gram-positive bacteria without internalization.

Zeta potential measurements that show that *cis* and *trans*-Azo-MoS$_2$ are exclusively interacting with the surface membrane of MRSA and not internalising can be used to correlate this conclusion. In case of *P. aeruginosa*, *cis* and *trans*-Azo-MoS$_2$ are not only interacting through electrostatic interaction but also internalizing into cells. The above date from zeta potential measurement and intracellular ROS generation can be summarized that *cis*-Azo-MoS$_2$ is more effective against MRSA due to targeting the membrane. However, *trans*-Azo-MoS$_2$ is more effective against *P. aeruginosa* due to more internalization followed by high intracellular ROS generation.

To further support the mechanism behind selective interaction, we formulated two different lipid vesicles to reliably mimic the Gram-positive and Gram-negative bacterial membranes.[63] For Gram-positive bacteria, phosphatidylglycerol (PG) and lipoteichoic acid (LTA) were used (9:1 molar ratio) to prepare vesicles (PG-LTA) (Figure 5a). For Gram-negative bacteria, the vesicle was composed of phosphatidylglycerol (PG) and cardiolipin (CL) (PG-CL, 9:1 in molar ratio) (Figure 5b). We assessed the binding thermodynamics of PG-LTA and PG-CL toward the *cis* and *trans*-Azo-MoS$_2$ using isothermal titration calorimetry (ITC). The PG-LTA and PG-CL vesicles were titrated into the *cis* and *trans*-Azo-MoS$_2$ in the working buffer. Depending on the functionalization of **Azo-MoS$_2$** material, different
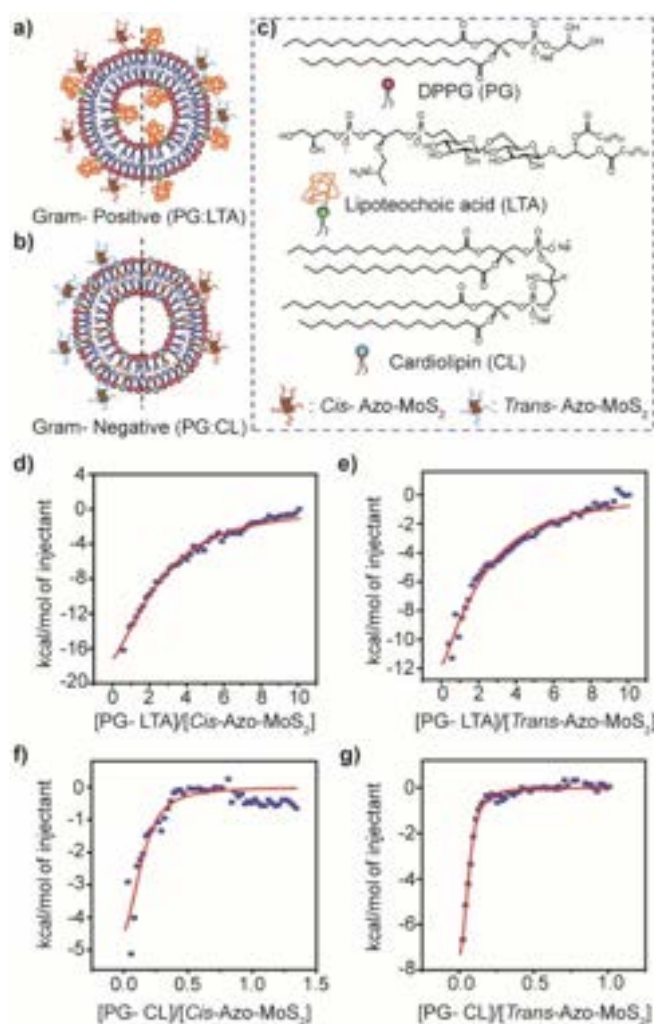
**Figure 5.** Isothermal titration calorimetry of **Azo-MoS₂** with Gram-positive and Gram-negative bacterial membrane mimicking lipid nanoparticles. (a, b) The schematic diagram of PG-LTA and PG-CL lipid nanoparticles. (c) The composition of both the lipid nanoparticles. Thermogram for titration of PG-LTA with (d) *cis*-Azo-MoS₂. (e) *trans*-Azo-MoS₂ and PG-CL with (f) *cis*-Azo-MoS₂. (g) *trans*-Azo-MoS₂.

thermodynamic binding constants were obtained (Figure 5). The complexation of **Azo-MoS₂**, both *cis* and *trans* functionalized, with PG-LTA and PG-CL were found to be exothermic in nature. Fitting the heat changes for PG-LTA using a one-site non-competitive binding model reveals that ***cis*-Azo-MoS₂** binds stronger than ***trans*-Azo-MoS₂** (Figure 5d&e). Comparatively higher heat change was observed

when PG-CL binds to ***trans*-Azo-MoS₂** than to ***cis*-Azo-MoS₂** (Figure 5f&g). A one-site binding model that assumes equivalent and non-cooperative binding was fitted to the thermograms. The isothermal curve fitting study yielded thermodynamic data, such as binding constants ($K_b$) and enthalpy changes ($\Delta H$), which are listed in the Table for each pair (Table 1). The binding was found to be primarily enthalpy driven.

The overall mechanistic investigation indicates that ***cis*-Azo-MoS₂** has shown high bactericidal activity against Gram-positive bacteria than ***trans*-Azo-MoS₂**. However, in case of Gram-negative bacteria, the ***trans*-Azo-MoS₂** was found to be more effective antibacterial agent than ***cis*-Azo-MoS₂**. The possible mechanistic pathway responsible for such selectivity was established. The membrane depolarization and membrane permeabilization are mainly responsible for high bactericidal activity of ***cis*-Azo-MoS₂** against Gram-positive bacteria. For Gram-negative bacteria, along with membrane depolarization and inner/outer membrane permeabilization, ***trans*-Azo-MoS₂** has exhibited intracellular ROS generation (Scheme 2a).

Therefore, we propose that the benzene ring with nitrogen in azo bond of ***cis*-Azo-MoS₂** interacts through hydrophobic and non-covalent interaction with the membrane of Gram-positive bacteria.[64–65] Additionally, the teichoic/lipoteichoic acid found in the cell walls of Gram-positive bacteria increases the rigidity of the wall by coordinating metal cations ($Na^+$, $K^+$ ions).[66] The effective coordination of these metal cations with azo nitrogen atoms most likely is responsible for the higher bactericidal activity compared to ***trans*-Azo-MoS₂**. Since Gram-negative bacteria have additional membranes, this non-covalent interaction can be attenuated. Apart from that, the Gram-negative bacteria have higher negative surface charge potential than Gram-positive ones and has extra inner membrane. The ***trans*-Azo-MoS₂** has shown higher activity due to strong electrostatic interaction with highly negatively charged bacteria membrane followed by internalization compared to ***cis*-Azo-MoS₂** due to exposed cationic head group.

### Cellular toxicity and histological evaluation

The toxicity assessment of functionalized 2D-MoS₂ should be estimated prior to in vivo study. The MTT assay was used to conduct a dose-dependent cellular toxicity investigation of the effects of *cis* and ***trans*-Azo-MoS₂** on the HeLa cell line. At high concentrations, azo functionalized 2D-MoS₂ was found to be toxic to HeLa cells (Figure S11a). At 5 μg/

**Table 1:** The thermodynamic parameters derived for **Azo-MoS₂** binding with PG-CL and PG-LTA.

| Titrant | Material | N | $K_b (M^{-1})$ | $\Delta H$ (kcal/mol) | $\Delta S$ (cal/mol/deg) |
|---------|----------|---|----------------|------------------------|---------------------------|
| PG-LTA | *Cis*-Azo-MoS₂ | 2.35 | $6.06 \times 10^4$ | -29.32 | -76.4 |
| | *Trans*-Azo-MoS₂ | 1.66 | $4.50 \times 10^4$ | -27.59 | -71.2 |
| PG-CL | *Cis*-Azo-MoS₂ | 0.136 | $1.12 \times 10^5$ | -6.36 | 1.78 |
| | *Trans*-Azo-MoS₂ | 0.059 | $5.09 \times 10^5$ | -9.93 | -7.19 |
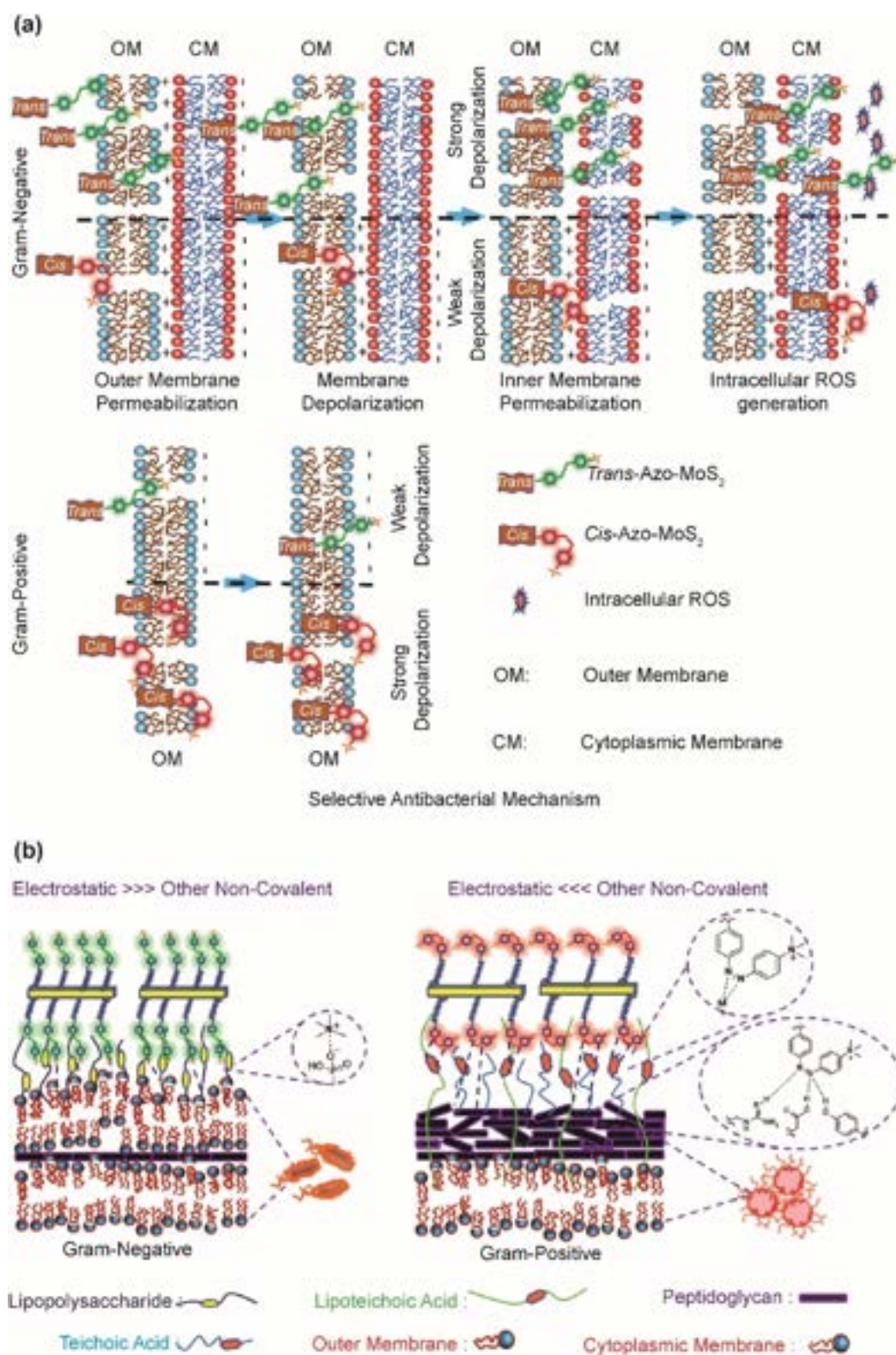
**Scheme 2.** (a) The mechanistic pathway for selective antibacterial activity of *cis* and *trans*-Azo-MoS₂ against Gram- negative and Gram-positive bacteria. (b) The pausible mechanistic pathway for selective antibacterial activity of *cis* and *trans*-Azo-MoS₂ against Gram- negative and Gram-positive bacteria.

mL, which is 10 times greater than the bactericidal concentration for MRSA and *P. aeruginosa*, we found very insignificant cytotoxicity. Additionally, we can see that the cytotoxicity of the *cis* and *trans*-Azo-MoS₂ does not differ

*Angew. Chem. Int. Ed.* **2024**, *63*, e202314804 (8 of 11)

© 2023 Wiley-VCH GmbH

much from one another. All these toxicity values indicate functionalized ce-MoS$_2$ elicits very low mammalian cellular toxicity. This is mainly due to the zwitterionic lipid membranes of mammalian cells.[67] Similar trend has been observed in other antimicrobial nanomaterials. The biocompatibility of **Azo-MoS$_2$** was evaluated through hemolysis and hematological analysis. The RBCs of a healthy donor was incubated with **Azo-MoS$_2$** at 37 $^0$C to characterize the hemolytic performance. It can be seen from Figure S11b that there is no hemolysis of RBCs with 10 mg/mL concentration of **Azo-MoS$_2$**. The absorbance of supernatant at 570 nm revealed that the hemolysis rate caused by **Azo-MoS$_2$** at 10 mg/mL is not different from the control (PBS). This concentration is 15 times higher than the minimum bactericidal concentration of **Azo-MoS$_2$**, indicating good biocompatibility.

### In Vivo treatment of bacteria infected wounds by Azo-MoS$_2$

Finally, we established a bacteria infected mouse wound model to determine the antibacterial effect of **Azo-MoS$_2$** in vivo (Figure 6a). A circular wound with a diameter $\approx 8$ mm was created on the back of balb/c mice. The wound was infected by adding the inoculate of MRSA bacteria. The wounds were treated with **cis-Azo-MoS$_2$**, **trans-Azo-MoS$_2$**, vancomycin, and PBS after being infected for 1 hour with MRSA. All antibacterial agents and vancomycin were used at 10×MBC. Vancomycin was used as the positive control for the treatment of wound. The wounds were monitored for 10 days. The images in Figure 6(b,d) demonstrate that after 10 days, neither vancomycin nor PBS were able to stop the bacteria from interfering with the wound healing procedure.

However, the process of wound closure was significantly improved by both the **cis** and **trans-Azo-MoS$_2$** treatments. Notably, **cis** treated mice healed much faster than **trans**, which is similar to the in vitro observation. The comparison of wound area values also illustrated the same. The number of bacteria that survive in wound tissue was also determined using the colony forming unit (CFU) method in order to visually quantify the inhibition of wound infection. The result shown in Figure 6(c,e), indicates that the number of bacterial colonies in the wound treated with **cis-Azo-MoS$_2$** was significantly decreased when compared to other treated and untreated wounds. The bacterial inhibition rate of **cis-Azo-MoS$_2$** and **trans-Azo-MoS$_2$** was higher than the known antibiotic vancomycin. The overall finding indicates that, in comparison to **trans** and positive control, **cis** functionalization has demonstrated superior antibacterial activity in both in vitro and in vivo system. At the same time, the in vivo biocompatibility of **Azo-MoS$_2$** was estimated using balb/c female mice as an animal model. The effect of **Azo-MoS$_2$** on main tissues of the mice was investigated.

Figure S12 represents the Hematoxylin (H) and eosin (E) staining in which major organs such as the heart, kidney, lungs, liver, and spleen of the treated mice did not suffer damage. Further, we evaluated the in vivo toxicity of **Azo-MoS$_2$**. PBS and **Azo-MoS$_2$** were applied on MRSA infected
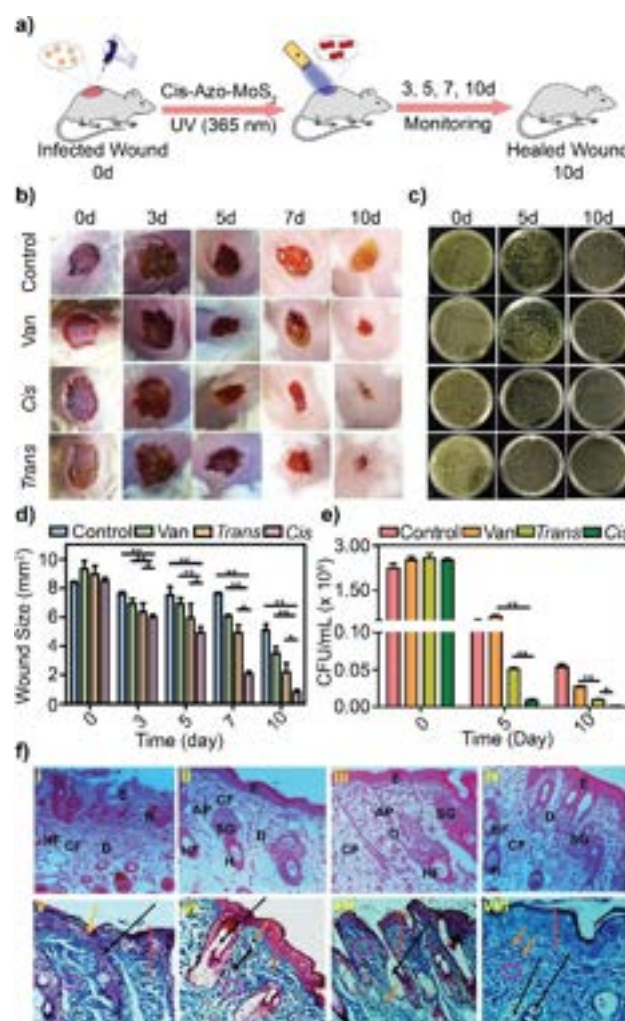
**Figure 6.** (a) Schematic diagram of wound infection model establishment, administration, and wound healing. (b) Photographs of MRSA (OD$\approx 0.1$) infected wounds on days 0, 3, 5, 7 and 10 without treatment and after treated with 10×MBC of **cis** and **trans-Azo-MoS$_2$** and vancomycin (Van) as positive control. (Van− 19.5 µg/mL, 25×MIC) (c) Photographs of agar plates during treatment on days 0, 5 and 10 to monitor the survival of bacteria on wound. (d) Measurement of wound size during treatment on days 0, 3, 5, 7 and 10 to compare the effective wound healing by **cis** and **trans-Azo-MoS$_2$**. (e) Survival rate of MRSA in the infected wound tissues using colony forming unit (CFU) method. ** denotes $P < 0.01$ with respect to control and Van. * denotes $p < 0.05$ with respect to **trans** (f) H and E staining method: Histological sections are magnified at 20X; (i) Control; (ii) Van (positive control); (iii) **cis-Azo-MoS$_2$**; (iv) **trans-Azo-MoS$_2$**; CF- Collagen fiber; N-Necrosis; SG- Sebaceous gland; AP- Arrector pili muscle; H-Hair; HF-Hair follicle. Masson trichrome stain of skin tissue at 20X; (v) Control; (vi) Van (positive control); (vii) **cis-Azo-MoS$_2$**; (viii) **trans-Azo-MoS$_2$**; red line (epidermic), yellow arrow (regeneration of wound tissue to new healed tissue), pink circle (collagen bundle arrangements), small black arrow (regeneration of collagen fibers from fibroblast), long black arrow (hair follicle), orange arrow (black coloured nuclei).

wound. On the 10$^{th}$ day after treatment, blood samples of the mice were collected for hematological analysis to determine the acute and chronic toxicities of **Azo-MoS$_2$**. As shown in Figure S13, the index of white blood cells (WBCs), red blood cells (RBCs), hemoglobin (HGB), hematocrit

(HCT), mean corpuscular volume (MCV), mean corpuscular hemoglobin (MCH), MCH concentration (MCHC), platelets (PLT) were all within the normal range compared with the control group, confirming non-damaging effect of **Azo-MoS₂** on the blood cells.

Besides, no significant inflammation in the body was observed upon treatment with **Azo-MoS₂**, further suggesting good biocompatibility of the system. To assess the wound healing capability, we conducted histological analysis of wound tissue. The H&E staining data in Figure 6f(i–iv) shows PBS treated wound tissue of control mice exhbiting the necrotic epidermis with striking bleeding and unorganised epidermal and dermal regions. Whereas mice treated with ***trans*-Azo-MoS₂** and positive control showed the repaired and organised epidermal and dermal layer with collagen fibers. Interestingly, ***cis*-Azo-MoS₂** treated mice showed more organised epidermis and dermis with collagen bundles.

Masson trichrome is a widely used technique to visualise the collagen tissues. The wounded skin stained with Masson trichrome provides an understanding of the wound healing process, as it illustrates the reorganisation of collagen fibres in the healed skin. The organised epidermis with four distinct layers such as stratum-basale, spinosum, granulosum and corneum exhibited fine collagen fibres in the ***cis*-Azo-MoS₂** treated group. While coarse to fine collagen fibres were observed in ***trans*-Azo-MoS₂** and positive control group, loosely filled collagen fibres with irregular arrangement were seen in the control group. Further, the Masson trichrome stain of skin tissue demonstrated proper wound healing with the native characteristics as shown in Figure 6f-(v–viii). The above studies demonstrate that the Azo-MoS₂ is non-toxic at the applied dosage with no side effects to skin tissue and other major organs. Notably, it helps generating high collagen in the treated wounds, which is responsible for faster healing. Overall, we confirm that this stimuli-responsive material is highly effective against infected wound healing applications.

## Conclusion

We have developed a 2D-MoS₂ based photoswitchable selective antibacterial agent which is capable of selective bactericidal activity in response to irradiation of UV or visible light due to *cis* and *trans* forms of **Azo-MoS₂**. For Gram-positive bacteria (MRSA), ***cis*-Azo-MoS₂** can have strong bactericidal activity while ***trans*-Azo-MoS₂** has shown effective killing against Gram-negative bacteria, *P. aeruginosa.* This selectivity can easily be controlled by switching the wavelengths of light irradiation. The selectivity of ***trans*-Azo-MoS₂** against *P. aeruginosa* originated from electrostatic interaction of the cationic group which is more exposed in *trans* conformation. On the other hand, hydrophobic interaction, hydrogen bonding, and metal ion coordination together play a key role in the selective bactericidal activity of ***cis*-Azo-MoS₂** against MRSA. Photoswitchable azobenzene-functionalized nanomaterials were applied for reversible cell adhesion and immobilization of bacteria but never explored in selective antibacterial activity. Notably, the low in vitro toxicity coupled with the non-hemolytic property of the material made it an ideal platform for wound healing application. Significantly, isomer-selective wound healing was observed along with faster healing than the commercially available antibiotics. Overall, this work provides a simple and efficient photoswitchable strain-selective bactericidal strategy, with a huge potential of efficacy against other microbial strains. The present study opens a new strategy to unleash the potential of azobenzene-functionalized nanomaterials with different core materials for various other biological applications such as bioimaging, controlled drug delivery and targeted therapy.

## Conflict of Interest

The authors declare no conflict of interest.

## Data Availability Statement

The data that support the findings of this study are available in the Supporting Information of this article.

[1] N. M. Alves, I. Pashkuleva, R. L. Reis, J. F. Mano, *Small* **2010**, *6*, 2208–2220.

[2] J. Brinkmann, E. Cavatorta, S. Sankaran, B. Schmidt, J. van Weerd, P. Jonkheijm, *Chem. Soc. Rev.* **2014**, *43*, 4449–4469.

[3] X. Liu, S. Wang, *Chem. Soc. Rev.* **2014**, *43*, 2385–2401.

[4] Q. Yu, Z. Wu, H. Chen, *Acta Biomater.* **2015**, *16*, 1–13.

[5] F. Wang, X. Sha, R. Wu, L. Zhang, X. Song, X. Tian, G. Pan, L. Liu, *Biomater. Sci.* **2021**, *9*, 5785–5790.

[6] D. Xu, J. Ricken, S. V. Wegner, *Chem. Eur. J.* **2020**, *26*, 9859–9863.

[7] Y. Zhou, Y. Zheng, T. Wei, Y. Qu, Y. Wang, W. Zhan, Y. Zhang, G. Pan, D. Li, Q. Yu, H. Chen, *ACS Appl. Mater. Interfaces* **2020**, *12*, 5447–5455.

[8] H. Liu, Y. Li, K. Sun, J. Fan, P. Zhang, J. Meng, S. Wang, L. Jiang, *J. Am. Chem. Soc.* **2013**, *135*, 7603–7609.

[9] H. Liu, X. Liu, J. Meng, P. Zhang, G. Yang, B. Su, K. Sun, L. Chen, D. Han, S. Wang, L. Jiang, *Adv. Mater.* **2013**, *25*, 922–927.

[10] K. H. Neoh, S. K. S. Cheng, H. Wu, A. Chen, Y. Sun, B. Li, A. Cao, R. P. S. Han, *ACS Appl. Nano Mater.* **2022**, *5*, 6911–6924.

[11] M. Liu, X. Wan, M. Yang, Z. Wang, H. Bao, B. Dai, H. Liu, S. Wang, *Angew. Chem. Int. Ed.* **2022**, *61*, e202114602.

[12] X. Liu, L. Chen, H. Liu, G. Yang, P. Zhang, D. Han, S. Wang, L. Jiang, *NPG Asia Mater.* **2013**, *5*, e63.

[13] L. Chen, X. Liu, B. Su, J. Li, L. Jiang, D. Han, S. Wang, *Adv. Mater.* **2011**, *23*, 4376–4380.

[14] X. Wei, K. Chen, B. Cai, L. Rao, Z. Wang, Y. Sun, M. Yu, W. Liu, S. Guo, X.-Z. Zhao, *ACS Appl. Mater. Interfaces* **2019**, *11*, 41118–41126.

[15] Q. Zhang, W. Wang, S. Huang, S. Yu, T. Tan, J.-R. Zhang, J.-J. Zhu, *Chem. Sci.* **2020**, *11*, 1948–1956.

[16] A. M. Ghafari, S. E. Domínguez, V. Järvinen, Z. Gounani, A. Schmit, M. Sjöqvist, C. Sahlgren, O. M. H. Salo-Ahen, C. Kvarnström, L. Torsi, R. Österbacka, *Adv. Mater. Interfaces* **2022**, *9*, 2101480.

[17] Y. Xiao, H. Zhou, N. Xuan, M. Cheng, Y. Rao, Y. Luo, B. Wang, R. Tang, *ACS Appl. Mater. Interfaces* **2014**, *6*, 20804–20811.

[18] J. Keyvan Rad, Z. Balzade, A. R. Mahdavian, *J. Photochem. Photobiol. C* **2022**, *51*, 100487.

[19] J. Zhang, S. H. D. Wong, X. Wu, H. Lei, M. Qin, P. Shi, W. Wang, L. Bian, Y. Cao, *Adv. Mater.* **2021**, *33*, 2105765.

[20] J. Borges, L. C. Rodrigues, R. L. Reis, J. F. Mano, *Adv. Funct. Mater.* **2014**, *24*, 5624–5648.

[21] D.-H. Qu, Q.-C. Wang, Q.-W. Zhang, X. Ma, H. Tian, *Chem. Rev.* **2015**, *115*, 7543–7588.

[22] W. Szymański, J. M. Beierle, H. A. V. Kistemaker, W. A. Velema, B. L. Feringa, *Chem. Rev.* **2013**, *113*, 6114–6178.

[23] Q. Bian, W. Wang, S. Wang, G. Wang, *ACS Appl. Mater. Interfaces* **2016**, *8*, 27360–27367.

[24] C. Honnigfort, L. Topp, N. García Rey, A. Heuer, B. Braunschweig, *J. Am. Chem. Soc.* **2022**, *144*, 4026–4038.

[25] L. Stricker, E.-C. Fritz, M. Peterlechner, N. L. Doltsinis, B. J. Ravoo, *J. Am. Chem. Soc.* **2016**, *138*, 4547–4554.

[26] H. Yang, B. Yuan, X. Zhang, O. A. Scherman, *Acc. Chem. Res.* **2014**, *47*, 2106–2115.

[27] D. Liu, Y. Xie, H. Shao, X. Jiang, *Angew. Chem. Int. Ed.* **2009**, *48*, 4406–4408.

[28] Y. Ni, D. Zhang, Y. Wang, X. He, J. He, H. Wu, J. Yuan, D. Sha, L. Che, J. Tan, J. Yang, *ACS Appl. Mater. Interfaces* **2021**, *13*, 14543–14551.

[29] Q. Shen, L. Liu, W. Zhang, *Langmuir* **2014**, *30*, 9361–9369.

[30] P. Wan, Y. Chen, Y. Xing, L. Chi, X. Zhang, *Langmuir* **2010**, *26*, 12515–12517.

[31] T. Wei, W. Zhan, Q. Yu, H. Chen, *ACS Appl. Mater. Interfaces* **2017**, *9*, 25767–25774.

[32] C. Cheng, S. Li, A. Thomas, N. A. Kotov, R. Haag, *Chem. Rev.* **2017**, *117*, 1826–1914.

[33] S. Szunerits, R. Boukherroub, *J. Mater. Chem. B* **2016**, *4*, 6892–6912.

[34] Y.-S. Guo, X.-D. Weng, B. Wu, Y.-F. Mi, B.-K. Zhu, Y.-L. Ji, Q.-F. An, C.-J. Gao, *J. Membr. Sci.* **2019**, *583*, 152–162.

[35] G. Ye, J. Lee, F. Perreault, M. Elimelech, *ACS Appl. Mater. Interfaces* **2015**, *7*, 23069–23079.

[36] S. Karunakaran, S. Pandit, B. Basu, M. De, *J. Am. Chem. Soc.* **2018**, *140*, 12634–12644.

[37] S. Pandit, S. Karunakaran, S. K. Boda, B. Basu, M. De, *ACS Appl. Mater. Interfaces* **2016**, *8*, 31567–31573.

[38] W. Zheng, Y. Jia, Y. Zhao, J. Zhang, Y. Xie, L. Wang, X. Zhao, X. Liu, R. Tang, W. Chen, X. Jiang, *Nano Lett.* **2021**, *21*, 1992–2000.

[39] H.-L. Zhang, Y.-B. Gao, J.-G. Gai, *J. Mater. Chem. A* **2018**, *6*, 6442–6454.

[40] C. Korupalli, C.-C. Huang, W.-C. Lin, W.-Y. Pan, P.-Y. Lin, W.-L. Wan, M.-J. Li, Y. Chang, H.-W. Sung, *Biomaterials* **2017**, *116*, 1–9.

[41] M. A. Schumacher, P. Balani, J. Min, N. B. Chinnam, S. Hansen, M. Vulić, K. Lewis, R. G. Brennan, *Nature* **2015**, *524*, 59–64.

[42] A. Gupta, S. Mumtaz, C.-H. Li, I. Hussain, V. M. Rotello, *Chem. Soc. Rev.* **2019**, *48*, 415–427.

[43] A. Mondal, M. De, *ACS Appl. Nano Mater.* **2021**, *4*, 13947–13954.

[44] T. Wei, Z. Tang, Q. Yu, H. Chen, *ACS Appl. Mater. Interfaces* **2017**, *9*, 37511–37523.

[45] T. Wei, W. Zhan, L. Cao, C. Hu, Y. Qu, Q. Yu, H. Chen, *ACS Appl. Mater. Interfaces* **2016**, *8*, 30048–30057.

[46] J. Borovička, W. J. Metheringham, L. A. Madden, C. D. Walton, S. D. Stoyanov, V. N. Paunov, *J. Am. Chem. Soc.* **2013**, *135*, 5282–5285.

[47] G. Fang, W. Li, X. Shen, J. M. Perez-Aguilar, Y. Chong, X. Gao, Z. Chai, C. Chen, C. Ge, R. Zhou, *Nat. Commun.* **2018**, *9*, 129.

[48] S. Lee, T. W. Kang, I.-J. Hwang, H.-I. Kim, S.-J. Jeon, D. Yim, C. Choi, W. Son, H. Kim, C.-S. Yang, H. Lee, J.-H. Kim, *J. Am. Chem. Soc.* **2021**, *143*, 14635–14645.

[49] J. Ma, K. Li, S. Gu, *RSC Adv.* **2022**, *12*, 4852–4864.

[50] J. Niu, L. Wang, T. Cui, Z. Wang, C. Zhao, J. Ren, X. Qu, *ACS Nano* **2021**, *15*, 15841–15849.

[51] J. Tang, Q. Chen, L. Xu, S. Zhang, L. Feng, L. Cheng, H. Xu, Z. Liu, R. Peng, *ACS Appl. Mater. Interfaces* **2013**, *5*, 3867–3874.

[52] C. R. Vickery, B. M. Wood, H. G. Morris, R. Losick, S. Walker, *J. Am. Chem. Soc.* **2018**, *140*, 876–879.

[53] P. P. Pillai, B. Kowalczyk, K. Kandere-Grzybowska, M. Borkowska, B. A. Grzybowski, *Angew. Chem. Int. Ed.* **2016**, *55*, 8610–8614.

[54] J. Sahoo, M. De, *J. Mater. Chem. B* **2022**, *10*, 4588–4594.

[55] X. Yang, J. Li, T. Liang, C. Ma, Y. Zhang, H. Chen, N. Hanagata, H. Su, M. Xu, *Nanoscale* **2014**, *6*, 10126–10133.

[56] A. Mondal, M. De, *Tungsten* **2022**, https://doi.org/10.1007/s42864-42022-00196-42869.

[57] P. Joensen, R. F. Frindt, S. R. Morrison, *Mater. Res. Bull.* **1986**, *21*, 457–461.

[58] S. S. Chou, M. De, J. Kim, S. Byun, C. Dykstra, J. Yu, J. Huang, V. P. Dravid, *J. Am. Chem. Soc.* **2013**, *135*, 4584–4587.

[59] H. W. Boucher, G. H. Talbot, J. S. Bradley, J. E. Edwards, D. Gilbert, L. B. Rice, M. Scheld, B. Spellberg, J. Bartlett, *Clin. Infect. Dis.* **2009**, *48*, 1–12.

[60] H. Wang, Z. Song, S. Li, Y. Wu, H. Han, *ACS Appl. Mater. Interfaces* **2019**, *11*, 32659–32669.

[61] A. P. Singh, P. Nicholls, *J. Biochem. Biophys. Methods* **1985**, *11*, 95–108.

[62] X. Zhu, X. Ji, N. Kong, Y. Chen, M. Mahmoudi, X. Xu, L. Ding, W. Tao, T. Cai, Y. Li, T. Gan, A. Barrett, Z. Bharwani, H. Chen, O. C. Farokhzad, *ACS Nano* **2018**, *12*, 2922–2938.

[63] B. Bharatiya, G. Wang, S. E. Rogers, J. S. Pedersen, S. Mann, W. H. Briscoe, *Colloids Surf. B* **2021**, *199*, 111551.

[64] S. Cho, Q. Wang, C. P. Swaminathan, D. Hesek, M. Lee, G.-J. Boons, S. Mobashery, R. A. Mariuzza, *Proc. Natl. Acad. Sci. USA* **2007**, *104*, 8761–8766.

[65] R. S. Munford, *Infect. Immun.* **2008**, *76*, 454–465.

[66] J. G. Swoboda, J. Campbell, T. C. Meredith, S. Walker, *ChemBioChem* **2010**, *11*, 35–45.

[67] D. S. S. M. Uppu, M. Bhowmik, S. Samaddar, J. Halder, *Chem. Commun.* **2016**, *52*, 4644–4647.

# Simultaneous Exfoliation and Functionalization of 2H-MoS₂ by Thiolated Surfactants: Applications in Enhanced Antibacterial Activity

Subbaraj Karunakaran, [ID] Subhendu Pandit, [ID] Bikramjit Basu, [ID] and Mrinmoy De*[ID]

Department of Organic Chemistry, Laboratory for Biomaterials, Materials Research Centre, Centre for Biosystems Science and Engineering, Indian Institute of Science, Bangalore 560012, India

**S** *Supporting Information*

**ABSTRACT:** Two-dimensional transition metal dichalcogenides (TMDs), such as MoS₂, generally exist in two different polymorphic structures, metallic (1T phase) and semiconducting (2H phase). In context of their wide spectrum of applications ranging from electronic to biomedicine, the aspects of ligand conjugation and solution processability are highly significant. In addition, the assessment of their antibacterial property and biocompatibility is equally important to explore their biomedical applications. Here we report a new method for the exfoliation and direct functionalization of 2H-MoS₂ using surfactant molecules with thiol functionality. We found that the exfoliated MoS₂ using thiolated ligands are functionalized with desired functionality and the processing scheme can be extended to other TMDs. Functionalized 2H-MoS₂ exhibits highly enhanced antibacterial efficiency compared to similarly functionalized metallic 1T-MoS₂ against pathogenic bacteria. The newly synthesized functionalized 2H-MoS₂ exhibits better hemocompatibility, which makes it suitable for in vivo applications. This convenient functionalization method opens the door for many other applications of functionalized semiconducting 2H-MoS₂ and other TMDs.
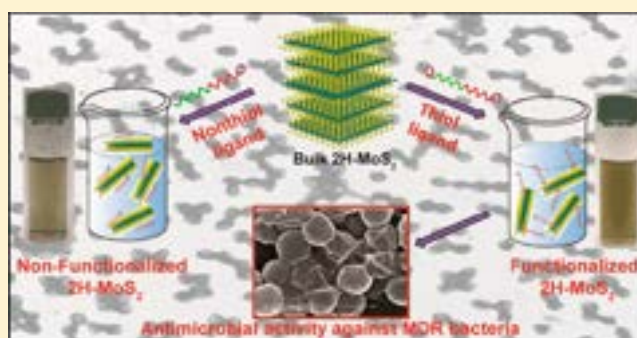
## ■ INTRODUCTION

Over the past few years, single-layer nanosheets of transition metal dichalcogenides (TMDs) have attracted great attention in many applications, ranging from electronics to sensing, catalysis, biomedical, energy storage, etc.[1−7] Layered TMDs are mainly present in two polymorphs (2H and 1T), depending on the coordination geometry of metal and chalcogen atoms. In the 2H structure, one metal atom is coordinated with six chalcogens in trigonal prismatic ($D_{3h}$) geometry with d-orbital splitting [$d_z^2$ (a1), $d_x^2-_y^2$, $d_{xy}$ (e), and $d_{xz,yz}$ (e′)], leading to semiconducting and photoluminescence property. In the 1T structure, the metal coordination is in the octahedral ($D_{3d}$) geometry with d-orbital splitting [$d_z^2$, $d_x^2-_y^2$ ($e_g$), and $d_{xy,xz,yz}$ ($t_{2g}$)], which results in the metallic character.[8−11] Depending on the inherent properties of those polymorphs, these kinds of materials are used for a wide spectrum of applications. For example, 1T-MoS₂ with metallic conductivity has been used in hydrogen evolution reaction (HER)[12] and cell destruction using near-infrared (NIR) photothermal effect.[13] On the other hand, 2H-MoS₂ with finite band gap and semiconducting property is utilized in wide-ranging applications, including electronic devices[14] and visible light-induced water disinfection.[15]

For many of the above applications, control over the preparation of 2H phase of MoS₂ with the desired functionalization poses a great challenge due to their inert nature, compared to 1T polymorph.[16,17] It is well-known that 1T TMDs are prepared in bulk quantities in solution by Li-intercalation method, using organolithium compounds such as n-butyl lithium or other alkali metal intercalating (sodium napthalenide).[18,19] Similarly, liquid-phase 2H TMDs are prepared by direct sonication of bulk materials in suitable solvents such as water, N-methyl pyrrolidine, isopropanol, etc.[20−23] Some surfactants or mixed-solvent assisted exfoliations are also utilized. For an example, ethanol in water can exfoliate and stabilize single to few layers of TMDs through their close surface energy.[24−28] Macromolecule-assisted exfoliations in the presence of chitosan, protein (BSA), and lignin are also reported.[29−31]

However, in all cases exfoliated 2H TMDs are not covalently functionalized, which may cause instability over time and limit their applications. In our earlier study, we had reported the covalent functionalization of 1T-MoS₂ by using thiol ligand, which was adopted for many applications.[32] The covalent functionalization has been reported to enhance the stability and applicability.[33−35] A few attempts of functionalizing 2H-MoS₂ using small thiolated molecules was reported involving a two-step method: layered 2H-MoS₂ preparation (solvent-assisted or physical vapor deposition) followed by conjugation

with a suitable ligand. However, these methods are limited by large-scale production and practical utility.[33,36–40] So far, small thiolated ligands, such as cysteine[41] and lipoic acid,[42] have been used for direct exfoliation and functionalization, but those resulted in multilayer TMDs. The mode of functionalization for cysteine is found to be physisorption, which compromises the extended stability. However, the utilization of thiolated surfactant for dual purpose, i.e., one-step process for exfoliation and direct functionalization of 2H-MoS$_2$, is limited. Herein, we hypothesized that surfactant thiol ligand with amphiphilic property could provide efficient exfoliation and functionalization of 2H-MoS$_2$ simultaneously (Figure 1a). In literature,
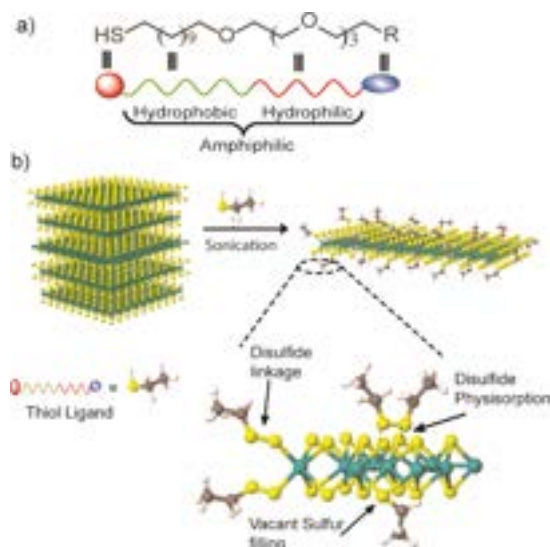


**Figure 1.** Scheme for the exfoliation of 2H-MoS$_2$ with amphiphilic ligand. (a) General ligand structure with amphiphilic nature composed of hydrophobic moieties near thiol (red circle) and hydrophilic tetraethylene glycol bearing functional group (blue oval). (b) Schematic representation of the ligand-induced exfoliation and possible modes of MoS$_2$ surface functionalization.

thiol surfactants have been extensively used as a stabilizer for noble nanomaterials like gold, platinum, etc.[43,44] Similar ligands also have been used to fabricate other nanomaterials such as CdSe.[44] However, the use of thiol surfactants in preparation of nanomaterials along with stabilization through functionalization has rarely been reported.[45] The thiol group present at the hydrophobic end of the ligand is likely to be anchored to the surface of MoS$_2$ as we observed earlier, and the desired headgroup at the hydrophilic end will introduce the suitable functionality in exfoliated materials (Figure 1b).

In this Article, we have used this novel strategy to exfoliate and functionalize 2H-MoS$_2$ using different thiol surfactants, providing long-term (>8 months) stability for the first time. Another novel aspect of the present work is to establish the enhanced bactericidal and biocompatibility of the functionalized 2H-MoS$_2$ solution. Following several research reports, nanomaterial-based antibiotics are emerging to combat multidrug-resistant bacteria.[46–52] Specifically, Liu et al. have shown that vertically aligned 2H-MoS$_2$ was used in water disinfection and exploited that semiconducting phase of the materials as a better reactive oxygen species (ROS) generator,[15] which inspired us to test the antibacterial activity. We have tested the ability of these functionalized materials toward antibacterial activity against Gram-positive and Gram-negative multidrug-

resistant bacteria. Interestingly, the positively charged 2H-MoS$_2$ shows better antibacterial activity with lower dosage even when compared to the similar positively charged 1T-MoS$_2$, which is known as a highly efficient antibacterial agent from our previous study.[53]

## RESULTS AND DISCUSSION

**Ligand-Induced Exfoliation of TMDs.** We have shown that thiolated ligand can functionalize the solution-processed 1T-MoS$_2$ and that it was adapted for various applications, such as making highly efficient antibiotics.[53] That method was further extended by several other groups for many more applications.[54–56] Hence, we have first considered three thiol surfactants with different charge-based headgroups according to the earlier reported method, due to their high biocompatibility and ability to impart stability to functionalized materials in biological media.[32,53] Also, to validate the importance of the thiol group, we have synthesized similar surfactants without a thiol group (Supporting Information, Figures S1–S4). In ligand design, we have used C-11 alkyl chain and tetraethylene glycol as a spacer to obtain a desirable combination of hydrophobicity and hydrophilicity. For negatively charged headgroup, we have considered carboxylate functionality. In addition, trimethylammonium and hydroxyl groups are used as positively charged and neutral headgroup, respectively (Figure 2a). Once all ligands were synthesized and characterized by NMR, they were used for exfoliation of bulk MoS$_2$ by the sonochemical method.
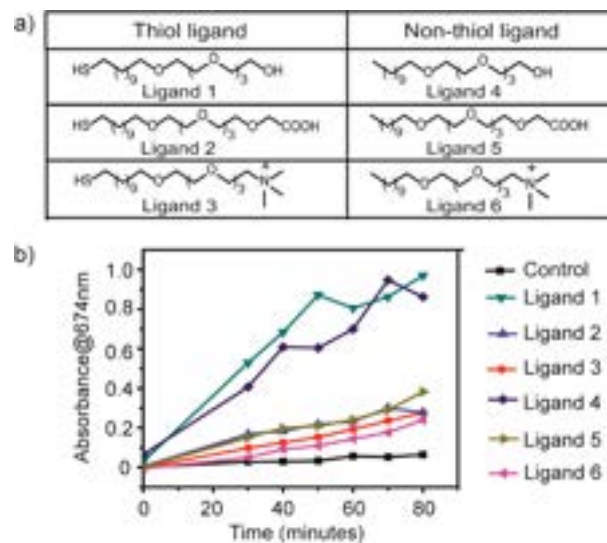


**Figure 2.** Monitoring ligand-dependent rate of exfoliation of MoS$_2$ by UV–vis spectroscopy. (a) Structure of amphiphilic thiol and nonthiol ligands with three differently charged headgroups utilized for exfoliation of the bulk MoS$_2$. (b) Temporal evolution of absorbance at 674 nm of exfoliated MoS$_2$ by thiol and nonthiol ligand with different time intervals of sonication.

In a typical sonochemical exfoliation experiment, 5 mg of bulk MoS$_2$ was added to 15 mL of aqueous solution containing 1.5 equiv of thiol and nonthiol ligands with respect to the molecular weight of MoS$_2$. This mixture was pulse-sonicated by probe sonicator over a period of 80 min, and the progress of exfoliation was monitored by UV–vis spectroscopy (Figure 2b), which correlates well with the amount of exfoliated MoS$_2$ in solution. The optimization of ligand concentration for

exfoliation was estimated by UV−vis spectroscopy (Figure S5). The spectroscopy result indicates that the absorbance evolution at 674 nm increases as the concentration of ligand increases from 0.5 to 1.5 equiv and remains saturated at 2 equiv. As shown in Figure 2b, different ligands exhibit different influences on the extent of exfoliation of bulk MoS$_2$, depending on their solubility and interaction through different head-groups. The neutral ligands (**ligand 1** and **ligand 4**) exfoliate better than the negatively charged ligands (**ligand 2** and **ligand 5**), followed by positive ligands (**ligand 3** and **ligand 6**). However, in all cases, the rate of exfoliation is higher in the presence of ligands compared to the control (no ligands), indicating the crucial role of ligands in disrupting the van der Waal force between two layers of MoS$_2$. The best exfoliation rate of **ligand 1** and **ligand 4** could be attributed to the hydrophobicity of the ligand compared to the charged ligands. The favorable interaction of neutral ligands with MoS$_2$ is distinctively observed during mixing the ligands and bulk MoS$_2$ (Figure S6). After sonication, further purification was done by centrifugation at 2000 rpm for 10 min. Finally, the samples were subjected to dialysis to remove the excess of ligands, followed by characterization of all samples.

The exfoliation of MoS$_2$ was conducted with both thiolated and nonthiolated ligands with the same headgroup, but interestingly we found that, between thiolated and non-thiolated ligands, there is no significant difference in the rate of exfoliation, as shown in Figure 2b. However, we have noted that the exfoliation of MoS$_2$ in the presence of thiol ligands results in high colloidal stability for an extended period of time (>8 months) compared to the nonthiolated ligands, where flocculation was observed after the dialysis (see Figure 3a). This is likely due to the fact that thiol ligands functionalize and stabilize the exfoliated MoS$_2$, preventing the aggregation. Because it is well-known that during exfoliation of MoS$_2$ sulfur deficiencies will be formed at edges, these sites can be easily occupied by thiol ligands, resulting in functionalization. Alternatively, the formation of sulfur−sulfur bond on the basal plane may also happen, as reported in earlier studies.[42] The presence and attachment of ligands are confirmed by $^1$H NMR (Figures S7−S9), where the triethylene glycol (TEG) linkage of ligands is exposed outside, exhibiting the strong $^1$H signal, but the hydrophobic carbons are buried inside, giving the very weak $^1$H signal. However, the nonthiolated ligands help in exfoliation but lack conjugation, owing to the absence of thiol. This observation is further confirmed by the zeta potential measurement (Figure 3b). The thiol ligand-induced exfoliated MoS$_2$ (after purification) shows corresponding charges according to the headgroup, but nonthiol ligand-induced exfoliated MoS$_2$ shows negative charges similar to nonfunctionalized MoS$_2$, as reported earlier.[32] This clearly indicates that the thiol ligands functionalize and stabilize the exfoliated MoS$_2$. Thermogravimetric analysis of functionalized 2H-MoS$_2$ (Figure S10) further supports the presence of attached ligands and indicates the presence of ~70% of the ligand by weight on the surface of 2H-MoS$_2$. X-ray diffraction (XRD) study was used to understand the mode of functionalization between edge versus basal plane. The XRD pattern (Figure 3c) indicates that functionalization mainly happened at the edges, because there is no change in (002) peak at 14.4° in all the functionalized MoS$_2$ when compared to JCPDS no. 37-1492 (14.34° for 2H-MoS$_2$) database.

Further characterization was then performed to ensure that the exfoliated materials are single layers and 2H phase. Atomic
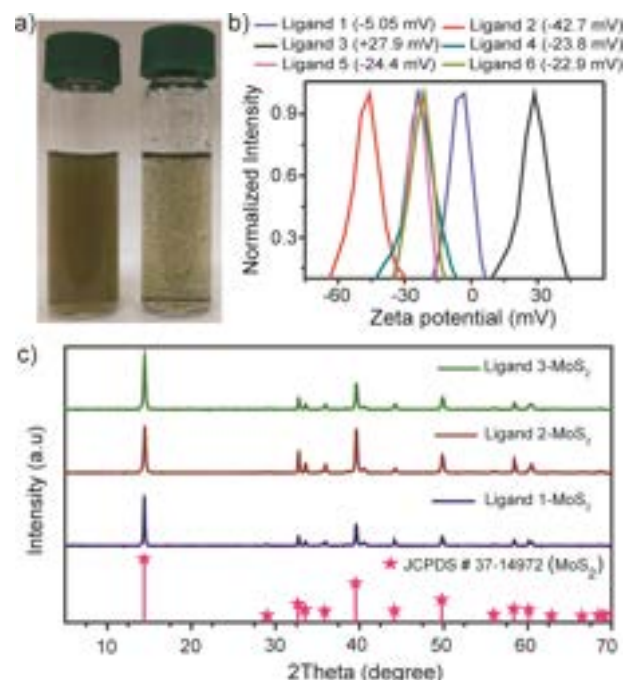


**Figure 3.** Stability of functionalized 2H-MoS$_2$ and understanding the mode of functionalization. (a) Colloidal stability of functionalized (**ligand 3**) and nonfunctionalized MoS$_2$ (**ligand 6**) over a period of >8 months. (b) Zeta potential of ligand-induced exfoliated MoS$_2$ by thiol ligands and nonthiol ligands. Different charges with thiol ligands indicate the surface functionalization. (c) X-ray diffraction (XRD) pattern of exfoliated MoS$_2$ by using thiol ligands which compared with JCPDS standard of MoS$_2$ indicates mode of functionalization is on the edges.

force microscopy (AFM) images of the exfoliated MoS$_2$ (by **ligand 3** as representative image) (Figure 4a) revealed that the exfoliated materials are single layers with height 1.5 nm along with the ligand, as shown in the height profile diagram (inset, Figure 4a). Further, UV−visible spectra show the presence of 2H-MoS$_2$ with A and B excitons peaks at 674 and 613 nm, which are attributed to the direct excitonic transitions at the K point of Brillouin zone. Also, indirect transition arises at Γ and Λ points in Brillouin zone from C and D excitons at 457 and 398 nm, which are present in contrast to the 1T-MoS$_2$ (Figure 4b).[57−59] The Raman spectra (Figure 4c) show a corresponding mode of vibration of 2H-MoS$_2$ (out-of-plane A$_1$g-384 and in-plane E$_2$g-409), with the absence of 1T associated peaks (at approximately J$_1$-157, J$_2$-226, and J$_3$-330 cm$^{-1}$) indicating predominantly 2H-MoS$_2$ was obtained by all the ligands.[60] The presence of 2D-flake nature of MoS$_2$ with average size 100−200 nm was confirmed by low-resolution transmission electron microscopy (TEM), as shown in Figure 4d. The high-resolution TEM (HRTEM) images (Figure 4e) indicate the layered nature, and zoomed inset images clearly showed the hexagonally symmetric structure of 2H-MoS$_2$.[30] Also, large-area HRTEM (Figure S11) could not reveal any evidence of structural distortion in the basal plane by this ligand-induced exfoliation, when compared to lithium-intercalated exfolia-tion.[61,62] The small-angle X-ray diffraction pattern (Figure 4f) indicates that single-crystalline nature is not affected during sonication.

Further, the exfoliated MoS$_2$ with different thiol ligands shows photoluminescence peaks at 670 nm (Figure S12), which confirms the 2H phase of MoS$_2$. The exfoliated MoS$_2$ by
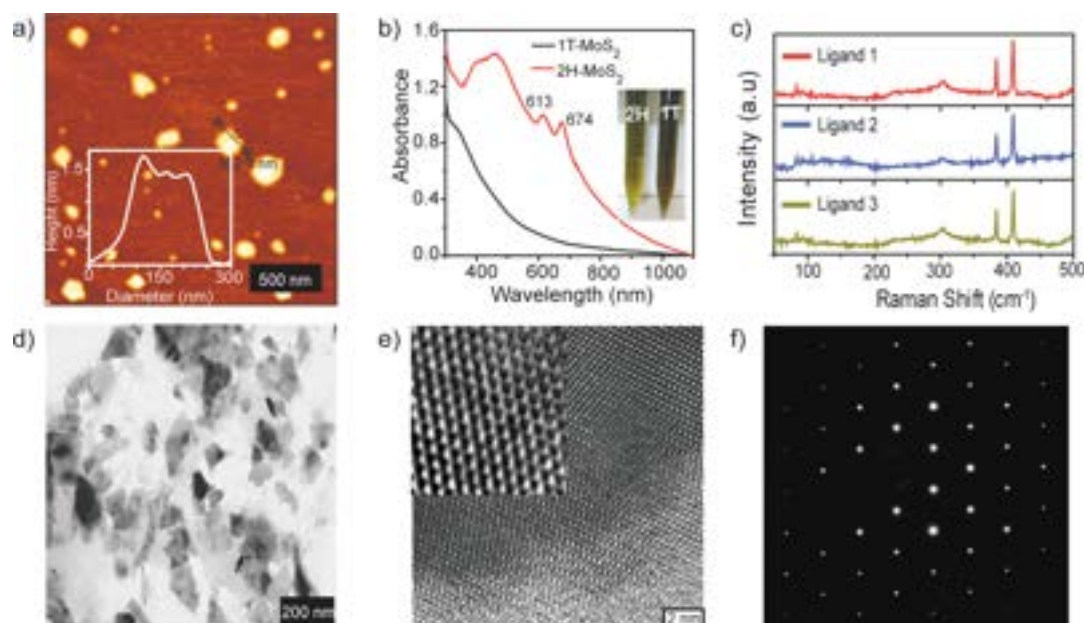
**Figure 4.** Characterization of 2H phase of MoS$_2$ and morphological characteristic of **ligand 3** functionalized MoS$_2$. (a) AFM image with inset height profile diagram indicates the formation of a single layer with functionalization. (b) Comparative UV−visible spectra of 1T-MoS$_2$ and 2H-MoS$_2$ indicate the presence of direct excitonic transitions in 2H phase. Inset picture presents the visual appearance of two different materials at the same concentration (1 mg/mL). (c) Raman spectra of exfoliated MoS$_2$ by different thiol ligands indicate the absence of 1T phase. (d−f) TEM, HRTEM, and small-angle X-ray diffraction pattern of functionalized MoS$_2$. Inset zoomed image indicates the hexagonal phase of 2H MoS$_2$.

**Table 1. MIC and MBC of Functionalized 2H-MoS$_2$ and Comparison with Functionalized 1T-MoS$_2$ against MRSA and *P. aeruginosa***

| 2H-MoS$_2$ | MRSA (MIC) | | *P. aeruginosa* (MIC) | | MRSA (MBC) | | *P. aeruginosa* (MBC) | |
|---|---|---|---|---|---|---|---|---|
| | 2H | 1T[a] | 2H | 1T[a] | 2H | 1T[a] | 2H | 1T[a] |
| control | >4.75 ppm | >15 ppm | >4.75 ppm | >15 ppm | NA | NA | NA | NA |
| ligand 1 | NI | NI | NI | NI | NA | NA | NA | NA |
| ligand 2 | NI | NI | NI | NI | NA | NA | NA | NA |
| ligand 3 | 297 ppb | 1.88 ppm | 594 ppb | >15 ppm | 297 ppb | 3.75 ppm | 4.75 ppm | NA |
| ligand 7 | 9.45 ppb | 156 ppb | 9.45 ppb | 156 ppb | 18.75 ppb | 156 ppb | 18.75 ppb | 156 ppb |
| ligand 8 | 9.45 ppb | 78 ppb | 9.45 ppb | 78 ppb | 9.45 ppb | 78 ppb | 9.45 ppb | 78 ppb |

[a]The value for 1T MoS$_2$ is adapted from our previous report.[53] In the table, concentration is expressed based on Mo only. No inhibition, NI; not applicable, NA.

various ligands and morphologies are also studied (Figures S13 and S14). Also, to test the versatility of our method we utilized **ligand 4** to exfoliate other TMDs (MoSe$_2$, WS$_2$, and WSe$_2$). It is found that this method is versatile for other TMDs, which is confirmed by AFM and TEM analysis (Figures S15 and S16). The concentration of exfoliated MoS$_2$ with different ligands was estimated by inductively coupled plasma mass spectrometry (ICP-MS). Thus, by using thiol surfactant, we efficiently exfoliated 2H-MoS$_2$ within a short period of time (∼1 h) with direct functionalization.

**Antibacterial Activity of Functionalized 2H-MoS$_2$.** It is evident that both 1T[63] and 2H phases[15] exhibit potential antibacterial activity and can be enhanced by many folds through surface functionalization (∼1000 times for 1T-MoS$_2$).[53] To explore the potential of the material core apart from surface functionalization, we have tested the antibacterial activity of the 2H functionalized materials. We have considered two different bacterial strains, Gram-positive *methicillin-resistant Staphylococcus aureus* (MRSA) and Gram-negative *Pseudomonas aeruginosa* (*P. aeruginosa*), as two representatives of ESKAPE pathogens (*Enterococcus faecium, Staphylococcus*

*aureus, Klebsiella pneumoniae, Acinetobacter baumannii, Pseudomonas aeruginosa*, and *Enterobacter* species). These pathogens are identified as most threatening pathogens by the Infectious Disease Society of America (IDSA) due to the rapid development of antibiotic resistance.[64] The minimum inhibitory concentration (MIC) of all 2H functionalized MoS$_2$ against bacteria was determined using broth dilution method with different concentrations of functionalized 2H-MoS$_2$. The detailed procedure and growth curves are mentioned in the Supporting Information (Figure S17). Among all functionalized 2H-MoS$_2$, only **ligand 3** functionalized positively charged 2H-MoS$_2$ shows antibacterial activity against both bacterial strains. However, unconjugated, neutral (**ligand 1** conjugated), and negative (**ligand 2** conjugated) 2H-MoS$_2$ do not shown any inhibitory action in our concentration range (Table 1). This result is consistent with our previous report of 1T functionalized MoS$_2$. However, positively charged 2H-MoS$_2$ shows antibacterial activity against both MRSA and *P. aeruginosa* with lower inhibitory concentration. Notably, positively charged 1T-MoS$_2$ did not show effective antibacterial activity against *P. aeruginosa*, but
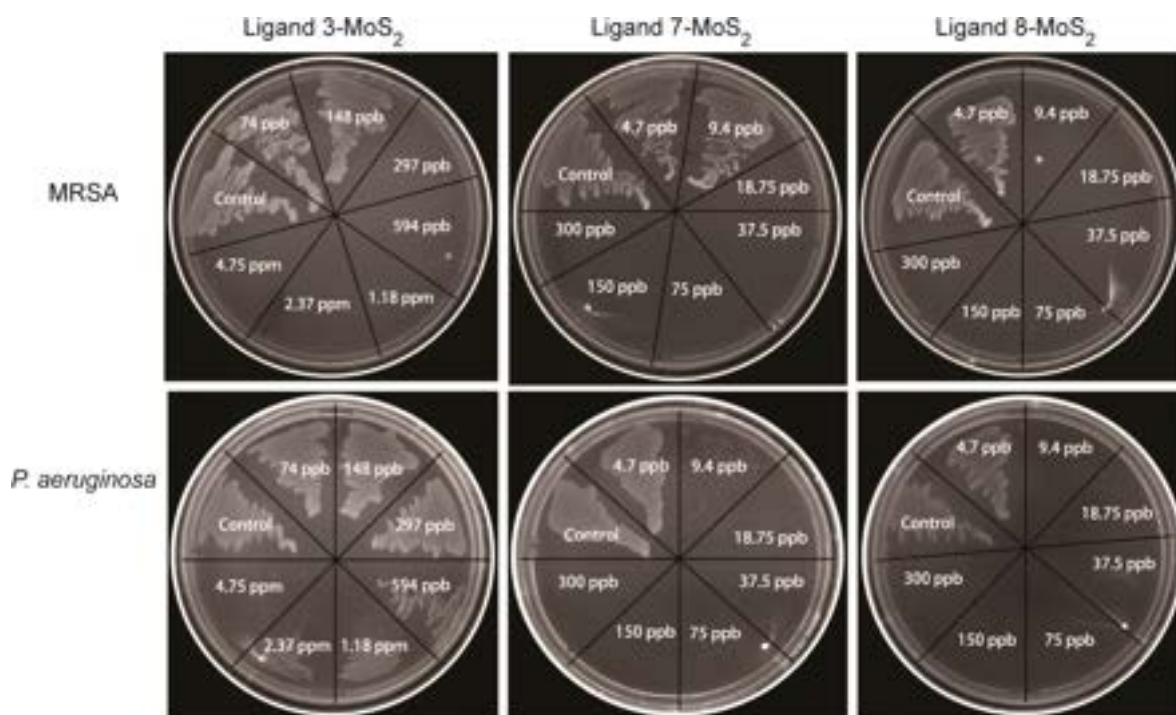
**Figure 5.** Colony-forming ability of MRSA and *P. aeruginosa* after treating with different positive MoS$_2$ for MBC estimation. The bacterial strains streaked on agar plate after 20 h incubation with positive MoS$_2$. The functionalized MoS$_2$ reduces the CFU of bacterial strain, in vitro.

positively charged 2H-MoS$_2$ exhibits relatively higher antibacterial activity against both strains of bacteria.

In our earlier study, we have also shown that, by increasing the hydrophobicity of positively charged MoS$_2$, we can improve the antibacterial activity by increased depolarization of the bacterial membrane.[53] Hence, to further enhance the antibacterial activity of 2H-MoS$_2$, we have prepared functionalized MoS$_2$ by cationic thiol ligand with increasing hydrophobicity, **ligand 7**-MoS$_2$ and **ligand 8**-MoS$_2$ (Figure 6a). Similar sonochemical method was used to prepare the functionalized 2H-MoS$_2$ using those ligands and confirmed by zeta potential measurement (Figure S18). As hypothesized, the **ligand 7** and **ligand 8** conjugated 2H-MoS$_2$ show enhanced antibacterial activity versus **ligand 3** conjugated 2H-MoS$_2$. Also, it was found that the MICs of MRSA and *P. aeruginosa* of 2H-MoS$_2$ conjugated with **ligand 3**, **ligand 7**, and **ligand 8** were 6.3 times, 16.5 times, and 8.25 times lower than that for the corresponding 1T-MoS$_2$, respectively. The minimum bactericidal concentration (MBC) is the complementary measurement to MIC. The MBC is the concentration at which the viability of bacteria is reduced to zero, which is generally estimated by quantifying colony-forming units in the agar plate. This infers that, even at MIC, the bacterial growth is inhibited but the microbial death may not happen. In that situation, plating the treated solution onto agar might still result in bacterial growth by colony formation. Hence, the MBC test will indicate the bactericidal effect of our newly developed antibiotics. We have found that functionalized 2H-MoS$_2$ is equally effective and notably better than 1T-MoS$_2$, as shown in Table 1 and Figure 5. As we can see from Figure 5, the colony-forming unit (CFU) is zero at MBC concentration. We have also observed in most cases that the MIC and MBC values are the same except the antibacterial activity of **ligand 3** functionalized 2H-MoS$_2$ against *P. aeruginosa* (10× concentration) and **ligand 7** functionalized 2H-MoS$_2$ against MRSA

(2× concentration). It is known that the antibacterial agents are considered bactericidal only if the MBC is <4 times the MIC. To this end, only **ligand 3** functionalized 2H-MoS$_2$ does not show bactericidal activity. Importantly, **ligand 8** functionalized 2H-MoS$_2$ shows similar bacteriostatic and bactericidal effect against both Gram-positive and Gram-negative bacteria. Further, the growth curve was used to extract the growth kinetics and doubling time (specific time interval between two subsequent binary fission), as reported by Rasool et al.[65] Tables S1 and S2 clearly show that there is no growth at the MIC in both the bacterial strain. This indicates the complete inhibition of bacterial function. The growth kinetics and doubling time are found only at very low concentrations as in **ligand 8**-MoS$_2$ (4.72 ppb), **ligand 6**-MoS$_2$ (4.72 ppb), and **ligand 3**-MoS$_2$ (148 ppb for MRSA and 296 ppb for *P. aeruginosa*). Even at the above-mentioned low concentrations, functionalized MoS$_2$ effectively reduces the growth rate and increases the doubling time of both strains, when compared to the control. For **ligand 8**-MoS$_2$ at 4.72 ppb treated MRSA, the growth rate is 0.288 h$^{-1}$ and the doubling time is 2.4 h. However, for control without MoS$_2$, the growth rate is 1.11 h$^{-1}$ and the doubling time is 0.6 h. Further, we have taken an effort to understand the effect of the free ligand on microbial toxicity. We have found that the free ligands (both with and without thiol) with a positively charged headgroup can also show antibacterial activity. However, the MIC value is very high compared to the functionalized MoS$_2$, which is estimated by bacterial growth curve analysis (Figure S19 and Table S3). This is an important finding because these ligands are widely used in gold and other nanomaterial functionalization and used as a potent antimicrobial agent against multidrug-resistant bacteria.[46] More significantly, the functionalized 2H-MoS$_2$ is found to be a more potent antibacterial agent with low dosage when compared to 1T-MoS$_2$, all-nanomaterial based antibacterial agent, and even small-molecule based antibiotics
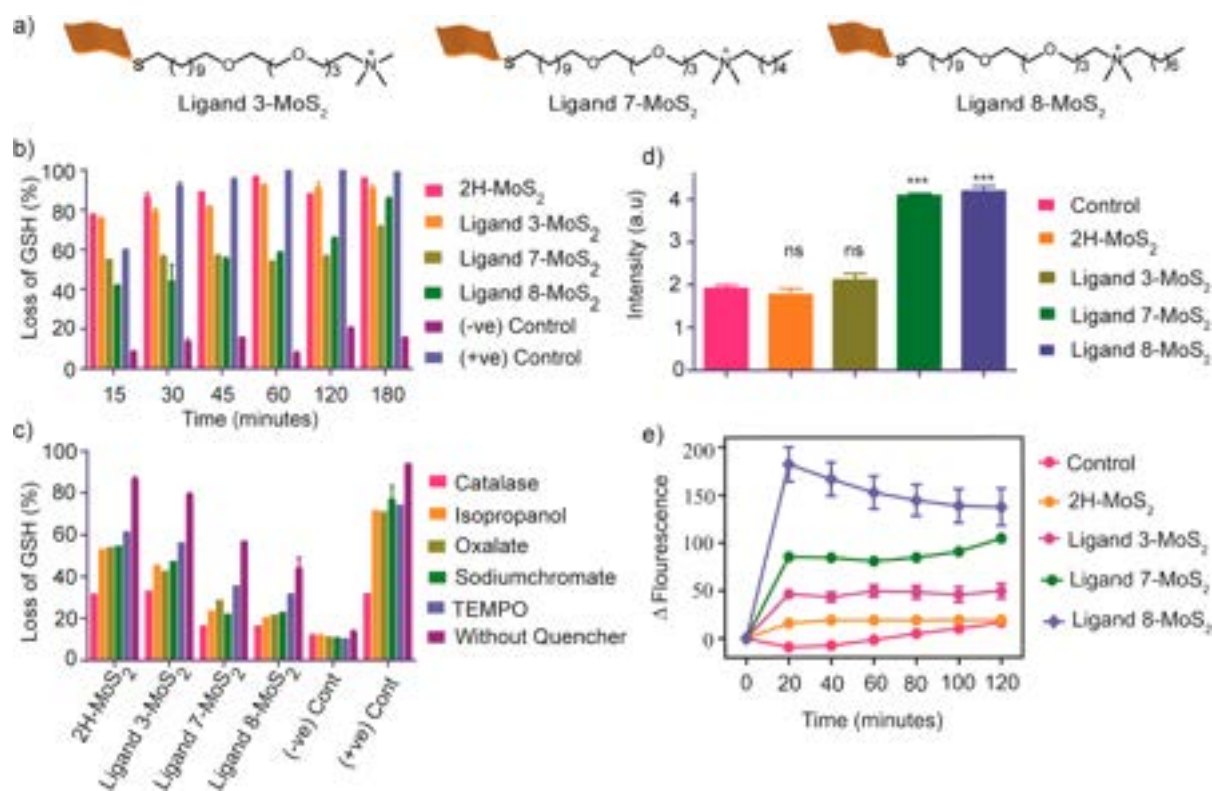
Figure 6. Mechanistic study for understanding the antibacterial property of functionalized $MoS_2$. (a) Structural representation of positively charged $MoS_2$ with varied hydrophobicities of **ligand 3**-$MoS_2$, **ligand 7**-$MoS_2$, and **ligand 8**-$MoS_2$. (b) Abiotic oxidative stress estimation by Ellman's assay with 0.4 mM glutathione, 10× MIC of functionalized $MoS_2$, and 1 mM of 5,5′-dithiobis(2-nitrobenzoic acid). The positive control is 10 mM $H_2O_2$ and without $MoS_2$ is considered as a negative control. All values are statistically significant ($P < 0.0001$) with respect to negative control. (c) Estimation of the type of ROS species by Ellman's assay in the presence of different ROS scavengers, 0.4 mM of isopropanol, oxalate, sodium chromate, (2,2,6,6-tetramethylpiperidin-1-yl)oxyl (TEMPO), and 10 $\mu$m of catalase. All the values with respect to that without quencher are statistically significant ($P < 0.0001$). (d) Intracellular ROS estimation with fluorescent probe 2′,7′-dichlorofluorescin diacetate (DCFDA) (2 mM) with MRSA with excitation wavelength 485 nm and emission wavelength 527 nm. **Ligand 7**- and **ligand 8**-$MoS_2$ are statistically significant (***$P < 0.0001$), and **ligand 3**-$MoS_2$ and 2H-$MoS_2$ are not significant (ns), with respect to control. (e) Quantification of membrane depolarization of MRSA. Pelleted MRSA stained with 50 $\mu$M 3,3′-dipropylthiadicarbocyanine iodide (DISC3(5)) fluorescent probe than added 10× MIC of 2H-$MoS_2$ and functionalized $MoS_2$. The fluorescence was monitored with an excitation wavelength of 622 nm and an emission wavelength of 670 nm.

(Figure S20). Also in view of the cost effectiveness, the starting material $MoS_2$ is very inexpensive ($0.4/g based on Sigma-Aldrich) compare to commonly used antibiotics such as Vancomycin ($150/g based on Sigma-Aldrich). Overall, this study clearly indicates that the positively charged 2H-$MoS_2$ is a better antibacterial agent compared to 1T-$MoS_2$. The enhanced activity most likely is due to the synergistic effect of 2H phase of the $MoS_2$ and the functionalized ligands.

**Mechanistic Study of the High Antibacterial Activity.** The high antibacterial activity of positively charged 2H-$MoS_2$ can be attributed by the two factors. The first one is that the core of the $MoS_2$ has a different phase, i.e., semiconducting 2H phase, which may cause enhanced oxidative stress. Another factor is the extent of ligand functionalization on the 2H-$MoS_2$, which is responsible for the membrane damage and hence results in enhanced activity. Liu et al. reported that vertically aligned 2H-$MoS_2$ generates various types of ROS,[15] which are playing the crucial role in the antibacterial activity. Hence, initially abiotic oxidative stress, mediated by functionalized 2H-$MoS_2$, was estimated by Ellman's assay. From Figure 6b, it is clear that 2H-$MoS_2$ results in more loss of glutathione (GSH) after 15 min (~78%), when compared to 1T-$MoS_2$ (~56%).[53] The smaller extent of ROS (may be peroxide) is plausibly generated in case of 1T-$MoS_2$ due to the electron transfer from

the biological sample to the oxygen via the metallic platform.[66] The suitable conduction band of 2H-$MoS_2$ (which is lower than the redox potential of selective ROS formation reaction) helps to generate many ROS species.[15] Hence, all positively charged 2H-$MoS_2$ are responsible for higher oxidative stress than that of similarly functionalized 1T-$MoS_2$.[53] Particularly after 15 min, **ligand 8** conjugated 2H-$MoS_2$ shows ~40% loss of GSH, while corresponding 1T-$MoS_2$ showed very negligible loss of GSH. Over the period of 3 h, the loss of GSH increases in both the 2H- and 1T-$MoS_2$ in a similar trend, but notably all 2H-$MoS_2$ results in more GSH loss compared to 1T-$MoS_2$, in vitro. Hence, this study clearly reveals that all positively charged 2H-$MoS_2$ generates more ROS than 1T-$MoS_2$.[53]

Further, to estimate the type of ROS species that are contributing to oxidative stress, we have used the different scavengers such as catalase (peroxide), isopropanol (hydroxyl radical), oxalate (hole), sodium chromate (electron), and TEMPO (superoxide anion radical) in Ellman's assay, as shown in Figure 6c. All the scavengers are effective in reducing GSH loss; particularly the catalase shows a high reduction of GSH loss. This clearly indicates that peroxide is one of the dominant species compared to all other investigated ROS species. It is consistently found that all fabricated 2H-$MoS_2$ in the presence of different scavengers causes a reduction in the
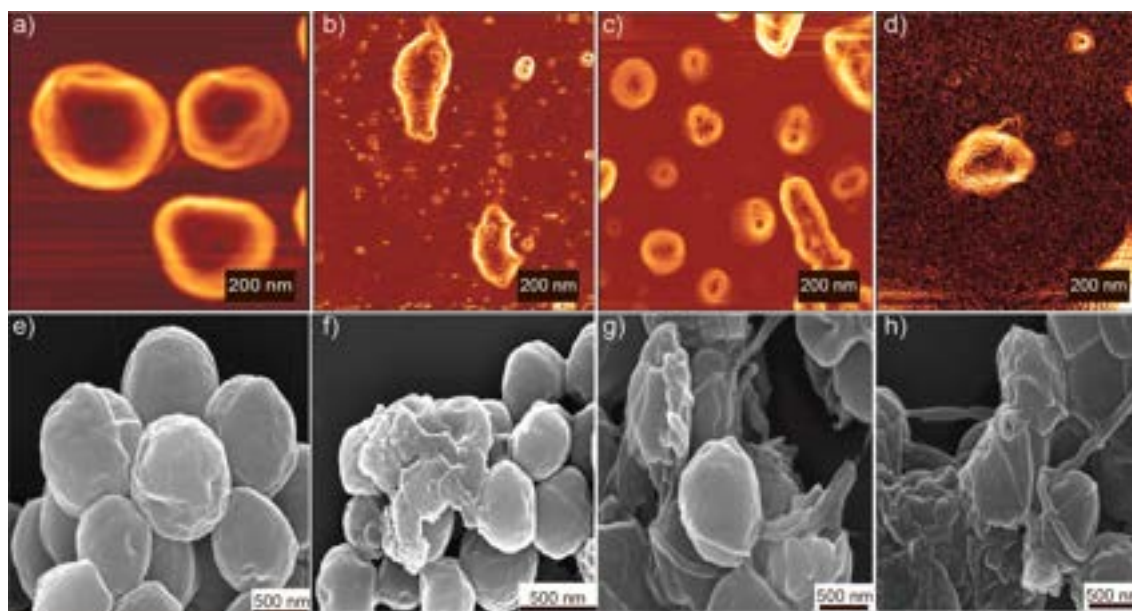
**Figure 7.** Morphological changes of MRSA after treatment with functionalized MoS$_2$ studied by AFM and SEM images. (a, e) Control only MRSA. (b, f) **Ligand 3**-MoS$_2$ treated MRSA. (c, g) **Ligand 7**-MoS$_2$ treated MRSA. (d, h) **Ligand 8**-MoS$_2$ treated MRSA. AFM and SEM images, respectively. The analysis provides signature of membrane alteration upon treatment with functionalized MoS$_2$.

loss of GSH. This indicates that ROS species are one of the important modes causing bactericidal property of positively charged 2H-MoS$_2$. We have also estimated the type of ROS generated by 1T-MoS$_2$ (Figure S21) for comparison. Interestingly we have found that only catalase shows the reduction in loss of GSH. Hence, peroxide is the only type of ROS species that is generated in 1T-MoS$_2$ due to the electron transfer from biological components.[66] Further, the fluorescent probe 2′,7′-dichlorofluorescin diacetate (DCFDA) is used to estimate the intracellular ROS generation by functionalized 2H-MoS$_2$. The dye (DCFDA) has cell-penetrating ability and can generate fluorescence in the presence of ROS species such as hydroxyl, peroxyl, etc. in the cell. The dye diffusion to the cell results in deacylation of DCFDA, and the following oxidation with ROS yields 2′,7′-dichlorofluorescein (DCF). DCF is a highly fluorescent compound that is used to estimate ROS by using fluorescence spectrometer with excitation and emission wavelengths of 485 and 527 nm, respectively. The intracellular ROS generation is found to be higher (Figure 6d) in **ligand 8**-MoS$_2$ and **ligand 7**-MoS$_2$ than in **ligand 3**-MoS$_2$. only 2H-MoS$_2$ does not have any significant enhancement when compared to the control (only dye). This may be attributed to the evidence that the positively charged functionalized 2H-MoS$_2$ can effectively interact with bacterial surface and leads to high intracellular ROS species. However, 2H-MoS$_2$ with negative charge is noninteractive, and hence no intercellular ROS was generated.

To probe the effect of 2H-MoS$_2$ with varied hydrophobicity on the bacterial membrane, we have assessed the membrane depolarization assay using 3,3′-dipropylthiadicarbocyanine iodide (DISC3(5)) fluorescent probe.[67] DISC3(5) is a lipophilic cationic dye that accumulates in the confined interior membrane of bacterial cells, as the surface possess net negative charge due to the presence of negatively charged component, such as teichoic acid. Aggregation within the confined membrane usually results in fluorescence self-quenching. Any material uptake results in membrane

depolarization causing release of dye, which can be easily estimated directly from fluorescence-enhancement study. Figure 6e indicates that the positively charged 2H-MoS$_2$ with higher hydrophobicity (**ligand 8**) shows greater membrane depolarization than intermediate (**ligand 7**) and least hydrophobic (**ligand 3**) functionalized 2H-MoS$_2$. Because highly hydrophobic MoS$_2$ strongly adheres to lipid components of microbial cell membranes, it results in disruption of the membrane. In contrast, only 2H-MoS$_2$ did not show any effect on membrane depolarization. In comparison to our previous report, the extent of membrane depolarization is very similar to the functionalized 1T-MoS$_2$. Thus, we can conclude from the above observation that the higher antibacterial activity of positively charged 2H-MoS$_2$ versus 1T-MoS$_2$ is mainly due to the elevated generation of various ROS species. However, the extent of membrane depolarization is similar, which is mainly attributed to externally functionalized ligands, which are the same in both types of MoS$_2$ materials. Thus, apart from external functionalization, the core of the material plays an important role in the bactericidal property.

Further, to support the mechanism visually, the change of membrane morphologies is imaged by atomic force microscopy (AFM) and scanning electron microscopy (SEM), as shown in Figure 7. Both AFM and SEM for untreated MRSA indicate clear spherical shape of bacteria with distinct membrane integrity (Figure 7a and e), whereas MRSA treated with **ligand 3** functionalized MoS$_2$ (Figure 7b and f) causes wrinkling with minimal damage due to masking of the bacterial membrane surface (resulting in oxidative stress). In contrast, **ligand 7** functionalized 2H-MoS$_2$ (Figure 7c and g) and **ligand 8** functionalized 2H-MoS$_2$ (Figure 7d and h) cause severe damage to the bacterial membrane and cause cell lysis. Transmission electron microscopy (TEM) images also support the effect of functionalized 2H-MoS$_2$ on bacterial-membrane integrity, which is composed of trilayer, plasma membrane followed by cell wall and the outer layer capsule.[68] It is evident from Figure 8a that the untreated *P. aeruginosa* has a rod-
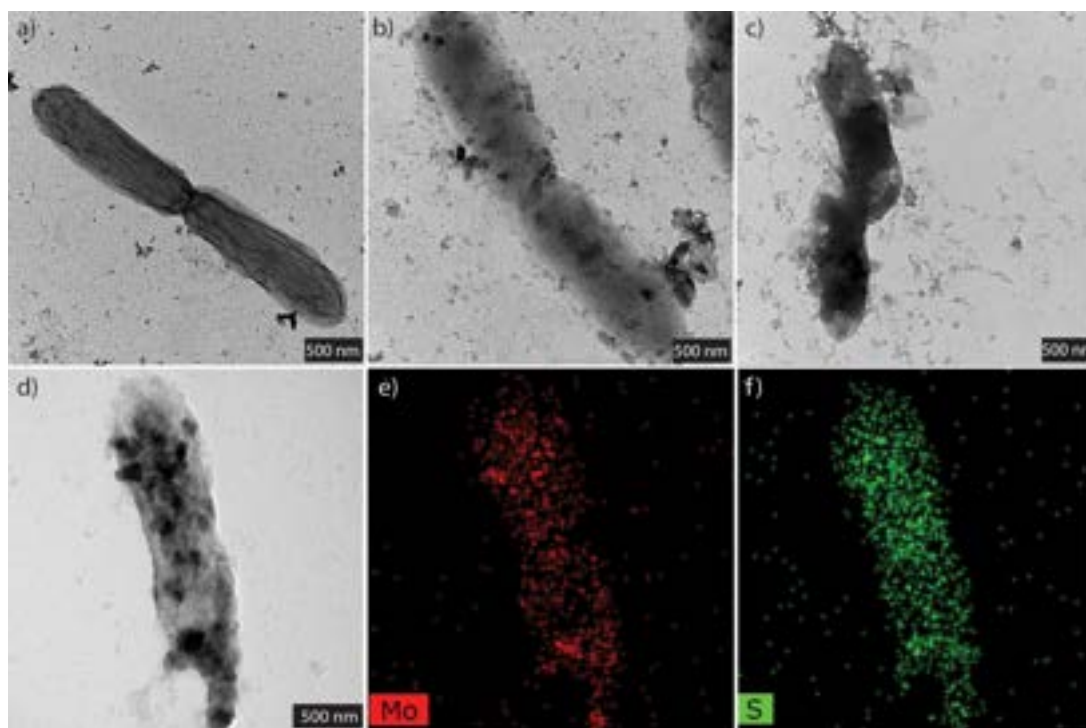
**Figure 8.** TEM-based analysis with elemental mapping of *P. aeruginosa*, which provides evidence for the interaction of functionalized MoS$_2$ with bacteria. (a) Control only *P. aeruginosa*. (b) **Ligand 3**-MoS$_2$ treated *P. aeruginosa*. (c) **Ligand 8**-MoS$_2$ treated *P. aeruginosa*. (d) **Ligand 3**-MoS$_2$ treated *P. aeruginosa*. (e) Elemental mapping of molybdenum in *P. aeruginosa* treated with **ligand 3**-MoS$_2$. (f) Elemental mapping of sulfur in *P. aeruginosa* treated with **ligand 3**-MoS$_2$.

shaped morphology with capsule layer, whereas **ligand 3**-MoS$_2$ treated strains show only binding at the outer membrane. This induces a loss in the capsule layer without any loss in membrane integrity due to the intact cell wall and plasma membranes (Figure 8b). However, **ligand 8**-MoS$_2$ results in complete damage of membrane (Figure 8c), and release of vital components from the cytoplasm (such as protein, ribosome, ATP, DNA, etc.) leads to the bacteriolysis. A similar effect was noted in MRSA treated with positively charged 2H-MoS$_2$ (Figure S22). Elemental mapping was carried out to locate the presence of MoS$_2$ in the treated sample. Parts e and f of Figure 8 clearly show the evidence for the presence of Mo and S on the *P. aeruginosa* externally as well as internally. The merged elemental mapping image and energy-dispersive spectroscopy (EDS) analysis further support the above observation (Figures S23 and S24). Hence, one can conclude that functionalized 2H-MoS$_2$ binds to the bacteria selectively, while inducing bacterial toxicity. The overall study concludes that **ligand 7** and **ligand 8** functionalized MoS$_2$ drive through the dual effect of membrane depolarization and oxidative stress, while **ligand 3** functionalized MoS$_2$ inhibits bacterial function only by ROS. Hence, the mechanism of the bactericidal property of 2H positively charged MoS$_2$ is mainly due to modulation/upregulation in oxidative stress with different ROS species and membrane depolarization.

**Hemocompatibility of Positively Charged 2H-MoS$_2$.** To test the biocompatibility of positively charged 2H-MoS$_2$, we performed hemolytic assay using rabbit erythrocytes. The in vitro hemolysis assay evaluates hemoglobin release (spectrophotometrically measured at 570 nm) in the plasma as an indicator of red blood lysis. In this protocol, isolated rabbit erythrocytes are incubated with functionalized positively charged 2H-MoS$_2$ for 1 h. Phosphate-buffered saline (PBS)

was used as negative control, and 0.1% of triton-X was used as positive control. After 1 h of incubation, intact erythrocytes are pelleted and the supernatants containing hemoglobin are released from lysed erythrocytes estimated photometrically by a plate reader at 570 nm. Experimentally, 8× concentrations of three functionalized 2H-MoS$_2$ exhibit minimal lysis to erythrocytes by the **ligand 3**-MoS$_2$ (2%), **ligand 7**-MoS$_2$ (4%), and **ligand 8**-MoS$_2$ (5%), as shown in Figure 9a. The functionalized MoS$_2$ with different concentrations on red blood cell (RBC) shows the absence of released hemoglobin (Figure 9b). This study indicates excellent hemocompatibility of functionalized 2H-MoS$_2$. Upon 24 h of incubation, only 8× MIC of all three positively charged 2H-MoS$_2$ are cytotoxic to rabbit erythrocytes (Figure S25).

Also, we have tested the hemolytic activity of free ligands at different time intervals. The result indicates, within a 1 h time frame, a significant amount of hemolysis noted with different free ligands (Figures S26 and S27). Hence, this study indicates that the grafting of ligands on MoS$_2$ considerably reduces the toxicity toward rabbit erythrocytes, compared to free ligands. This can be well-attributed to the known property of nanomaterials-based drugs to reduce nonspecific systemic toxicity. This highlights the importance of functionalized nanomaterials toward biological applications. Also, the enhanced antibacterial activity and in vitro biocompatibility of the reported materials prompt us to explore the possible in vivo aptness and related applications, which are currently in progress.

■ **CONCLUSION**

In summary, we have demonstrated that exfoliation and desired functionalization of 2H MoS$_2$ could be achieved efficiently within a short period of time using thiol surfactant in
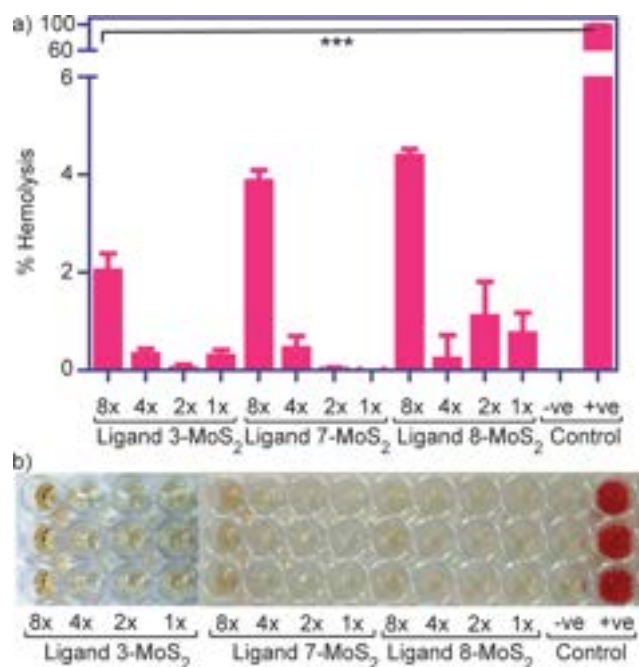
**Figure 9.** Hemocompatibility of functionalized 2H-MoS$_2$. (a) Hemolysis assay of positively charged 2H-MoS$_2$, all the values are statistically significant (***$P$ < 0.0001) with respect to positive control. (b) functionalized MoS$_2$ incubated with RBC centrifuged and collected supernatant to detect cell-free hemoglobin after 1 h of incubation. For negative control, only PBS was used without MoS$_2$, and 0.1% of TritonX-100 was used as positive control.

the sonochemical method. The effect of surfactant was illustrated using nonthiolated ligands, which only assisted in exfoliation but without functionalization. We have also demonstrated that this method can be extended to other TMDs for further applications in many fundamental studies. As an example, we have quantified the antibacterial activity of functionalized 2H-MoS$_2$ and compared it with the 1T phase of the same material. We have found that the positively charged 2H-MoS$_2$ exhibits higher antibacterial activity compared to the similarly functionalized 1T-MoS$_2$. Additionally, increasing the hydrophobicity in the positive headgroup can enhance the antibacterial activity by enhancing cell membrane depolarization. The mechanistic study indicates that the ROS-induced oxidative stress is more in 2H-MoS$_2$ when compared to 1T-MoS$_2$ due to the semiconducting nature of the 2H phase. However, the extent of membrane depolarization remains the same in both types of MoS$_2$ because the external functionalization remains the same as in 1T-MoS$_2$. Thus, we have concluded that a change in the core material also can enhance the antibacterial activity along with the surface modification in nanoantibiotics. This fundamental study on the alteration of core material, as well as surface functionality with 2D scaffold, can offer an opportunity for developing new materials toward many promising applications in protein recognition, delivery, imaging, and therapy. Current studies are underway to explore the possible use of these materials for in vivo applications such as cutaneous wound healing.

## ■ EXPERIMENTAL SECTION

**Inductively Coupled Plasma Mass Spectrometry for Mo Concentration Determination.** ICP-MS was analyzed using quadrupole inductively coupled plasma mass spectrometer. The unknown samples for analysis were prepared by adding 100 $\mu$L of

concentrated HNO$_3$ in a 15 mL vial containing 50 $\mu$L of functionalized material and incubated overnight at 100 °C for digestion. The digested samples were made up to 10 mL by adding DI water. Ammonium heptamolybdate (NH$_4$)$_6$Mo$_7$O$_{24}$·4H$_2$O was used to prepare known concentrations of Mo as an external standard. The external standards accuracy used for ICP-MS was confirmed by the linear regression fit to inductively coupled plasma mass spectrometry (ICP-MS) values of external standards ($R^2$ > 99.99). The molybdenum concentration of the stock solution was determined by multiplying the dilution factor, consistent with the procedure described earlier.

**Estimation of Oxidative Stress and Types of Reactive Oxygen Species Generated by Functionalized MoS$_2$.** Oxidative stress induced by functionalized MoS$_2$ was studied by Ellman's assay. In the procedure, 10× MIC of MRSA was used, that is, positive **ligand 3, 7,** and **8** conjugated MoS$_2$ and 3 ppm of 2H-MoS$_2$ were taken in a vial. Then 0.4 mM GSH was added, which was then dissolved in 50 mM bicarbonate buffer with pH 8.6. In the negative control, no MoS$_2$ was added, and in the positive control, 10 mM H$_2$O$_2$ was added. The tubes were wrapped with aluminum foils to prevent any photochemical oxidation, and solutions were incubated at 37 °C. From the stock at different time intervals (15 min, 30 min, 45 min, 1 h, 2 h, and 3 h), 100 $\mu$L of solution was added to 100 $\mu$L of 2 mM 5,5′-dithiobis(2-nitrobenzoic acid) (DTNB, SRL Chem) in 50 mM TRIS-HCl (pH 8.3, SRL Chem) buffer taken in a 96-well plate. Then the absorbance of the resulting solution was measured immediately after 5 min at 412 nm using a UV−visible spectrometer by plate reader.

The percentage loss of glutathione was calculated as

$$\left( 1 - \frac{\text{absorbance at 412 nm of the sample at a particular time}}{\text{absorbance at 412 nm of negative control at 0 min}} \right)$$
$$\times \, 100\%$$

For reactive oxygen species (ROS) estimation, the experimental procedure is exactly similar to that of Ellman's assay, but the only difference is that the assay is conducted in the presence of different quenchers added to the vial containing glutathione and 10× MIC MoS$_2$, such as hole-quencher sodium oxalate (0.4 mM), electron-quencher sodium chromate (0.4 mM), superoxide anion radical-quencher TEMPO (0.4 mM), peroxide-quencher catalase (1 $\mu$M), and hydroxyl radical-quencher isopropanol (0.4 mM). The reduction in the percentage loss of GSH in the presence of respective quencher implies the type of ROS species responsible for the oxidative stress of 2H-MoS$_2$. The concentrations of all the quenchers mentioned are the final concentrations.

**Intracellular ROS Study with DCFDA Probe.** The mid log phase culture ($A_{600nm} \approx 0.5$) of bacteria was harvested and suspended in PBS buffer. Then 20 $\mu$L of 100 mM DCFDA dye in dimethylsulfoxide (DMSO) was added to 1 mL of bacterial suspension. Also, 100 $\mu$L of bacteria was added to the 96-well plate, and 1 ppm of functionalized MoS$_2$ and nonfunctionalized MoS$_2$ were also added. The sample without MoS$_2$ is considered as the control. The experiments were performed in triplicate. The fluorescence was monitored with an excitation wavelength of 485 nm and an emission wavelength of 527 nm, for a period of 3 h with a lag time of 15 min. An increase in fluorescence indicates ROS generation in the presence of materials.

**Estimation of Membrane Depolarization Affinity of Functionalized MoS$_2$.** For quantification of membrane depolarization of bacteria by this functionalized MoS$_2$, the MRSA was harvested at mid log phase culture ($A_{600nm} \approx 0.3$) and centrifuged at 5000 rpm for 5 min. The pellet was washed with 5 mM glucose and 5 mM HEPES buffer (pH 7.2) mixed in 1:1 ratio, and the washed pellet was resuspended in 5 mM HEPES buffer, 5 mM glucose, and 100 mM KCl solution mixed in a 1:1:1 ratio. Then 100 $\mu$L of bacterial suspension was taken in a 96-well plate, 2 $\mu$L of 5 mM DISC3 dye (3,3′-dipropylthiadicarbocyanine iodide, TCI Chemicals) was added, and the plate was incubated for 30 min. Then 10× MIC of positive **ligand 3, 7,** and **8** conjugated MoS$_2$ and 3 ppm 2H-MoS$_2$ were added to the 96-well plate containing bacterial suspension and DISC3 dye.

After addition of the $MoS_2$, the fluorescence was monitored with an excitation wavelength of 622 nm and an emission wavelength of 670 nm, for the next 2 h with a lag time of 10 min. An increase in fluorescence indicates membrane depolarization of the bacterial membrane. The increase in fluorescence at a certain time compared to zero min has been taken and plotted.

**TEM Sample Preparation for Bacteria Imaging.** The bacteria were harvested at mid log phase with optical density (OD) ≈ 0.5, washed with PBS thrice, and suspended in PBS buffer. Then functionalized $MoS_2$ was added with a concentration equivalent to MIC, and it was incubated in a 37 °C shaking incubator. Then 3.5 μL bacterial suspension was incubated in UV treated carbon-coated copper for 30 sec and negative staining was performed using 0.75% uranyl acetate. The image acquisition was performed at 120 kV using the Tecnai T12 TEM and side-mounted Olympus VELITA CCD camera.

**Characterization.** UV–vis–NIR spectrophotometer (Shimadzu UV–vis–NIR spectrophotometer), Zeta Potential (Malvern Zetasizer Nano UK), XRD (Bruker X-ray diffractometer D8 Advance), fluorescence measurement (Thermo Scientific Varioskan Flash Multimode Reader), bacterial optical density (Eppendorf Bio Spectrometer UV–vis spectrometer), AFM (JPK instruments), Raman and photoluminescence (LabRAM HR), TEM (200 kV, FETEM) for TMDs characterization, FEI Titan Themis (300 kV) for EDS and elemental mapping (CeNSE, IISc) , FEI Tecnai T12 BioTwin 120kV TEM (Central Facility, Division of Biological Science, IISc) for bacteria imaging, and SEM (FEI Sirion XL30 FEG SEM) were used.

## ASSOCIATED CONTENT

### Ⓢ Supporting Information

The Supporting Information is available free of charge on the ACS Publications website at DOI: 10.1021/jacs.8b08994.

Synthetic procedure of nonthiol ligand, ligand optimization, NMR of ligand conjugated $MoS_2$, AFM and SEM of TMDs, photoluminescence, MIC, zeta potential, growth kinetics, doubling time, ROS quenching study, TEM of MRSA, elemental mapping and EDS spectra, and hemolytic assay (PDF)

## AUTHOR INFORMATION

### Corresponding Author

*md@iisc.ac.in

### ORCID Ⓘ

Subbaraj Karunakaran: 0000-0001-5093-490X
Subhendu Pandit: 0000-0002-4542-2069
Bikramjit Basu: 0000-0002-9154-5553
Mrinmoy De: 0000-0001-8394-9059

### Notes

The authors declare no competing financial interest.

## ACKNOWLEDGMENTS

## REFERENCES

(1) Nicolosi, V.; Chhowalla, M.; Kanatzidis, M. G.; Strano, M. S.; Coleman, J. N. *Science* **2013**, *340*, 1226419.
(2) Chhowalla, M.; Shin, H. S.; Eda, G.; Li, L.-J.; Loh, K. P.; Zhang, H. *Nat. Chem.* **2013**, *5*, 263.
(3) Choi, W.; Choudhary, N.; Han, G. H.; Park, J.; Akinwande, D.; Lee, Y. H. *Mater. Today* **2017**, *20*, 116.
(4) Lv, R.; Robinson, J. A.; Schaak, R. E.; Sun, D.; Sun, Y. F.; Mallouk, T. E.; Terrones, M. *Acc. Chem. Res.* **2015**, *48*, 56.
(5) Jariwala, D.; Sangwan, V. K.; Lauhon, L. J.; Marks, T. J.; Hersam, M. C. *ACS Nano* **2014**, *8*, 1102.
(6) Wang, Z. Y.; Mi, B. X. *Environ. Sci. Technol.* **2017**, *51*, 8229.
(7) Girish, Y. R.; Biswas, R.; De, M. *Chem. - Eur. J.* **2018** DOI: 10.1002/chem.201802468.
(8) Mattheiss, L. F. *Phys. Rev. B* **1973**, *8*, 3719.
(9) Fleischauer, P. D.; Lince, J. R.; Bertrand, P. A.; Bauer, R. *Langmuir* **1989**, *5*, 1009.
(10) Chhowalla, M.; Shin, H. S.; Eda, G.; Li, L. J.; Loh, K. P.; Zhang, H. *Nat. Chem.* **2013**, *5*, 263.
(11) Kan, M.; Wang, J. Y.; Li, X. W.; Zhang, S. H.; Li, Y. W.; Kawazoe, Y.; Sun, Q.; Jena, P. *J. Phys. Chem. C* **2014**, *118*, 1515.
(12) Lukowski, M. A.; Daniel, A. S.; Meng, F.; Forticaux, A.; Li, L.; Jin, S. *J. Am. Chem. Soc.* **2013**, *135*, 10274.
(13) Chou, S. S.; Kaehr, B.; Kim, J.; Foley, B. M.; De, M.; Hopkins, P. E.; Huang, J.; Brinker, C. J.; Dravid, V. P. *Angew. Chem., Int. Ed.* **2013**, *52*, 4160.
(14) Lee, K.; Kim, H. Y.; Lotya, M.; Coleman, J. N.; Kim, G. T.; Duesberg, G. S. *Adv. Mater.* **2011**, *23*, 4178.
(15) Liu, C.; Kong, D. S.; Hsu, P. C.; Yuan, H. T.; Lee, H. W.; Liu, Y. Y.; Wang, H. T.; Wang, S.; Yan, K.; Lin, D. C.; Maraccini, P. A.; Parker, K. M.; Boehm, A. B.; Cui, Y. *Nat. Nanotechnol.* **2016**, *11*, 1098.
(16) Voiry, D.; Goswami, A.; Kappera, R.; Silva, C. D. C. E.; Kaplan, D.; Fujita, T.; Chen, M. W.; Asefa, T.; Chhowalla, M. *Nat. Chem.* **2015**, *7*, 45.
(17) Chen, X.; McDonald, A. R. *Adv. Mater.* **2016**, *28*, 5738.
(18) Joensen, P.; Frindt, R. F.; Morrison, S. R. *Mater. Res. Bull.* **1986**, *21*, 457.
(19) Zheng, J.; Zhang, H.; Dong, S. H.; Liu, Y. P.; Tai Nai, C.; Suk Shin, H.; Young Jeong, H.; Liu, B.; Ping Loh, K. *Nat. Commun.* **2014**, *5*, 2995.
(20) Coleman, J. N.; Lotya, M.; O'Neill, A.; Bergin, S. D.; King, P. J.; Khan, U.; Young, K.; Gaucher, A.; De, S.; Smith, R. J.; Shvets, I. V.; Arora, S. K.; Stanton, G.; Kim, H. Y.; Lee, K.; Kim, G. T.; Duesberg, G. S.; Hallam, T.; Boland, J. J.; Wang, J. J.; Donegan, J. F.; Grunlan, J. C.; Moriarty, G.; Shmeliov, A.; Nicholls, R. J.; Perkins, J. M.; Grieveson, E. M.; Theuwissen, K.; McComb, D. W.; Nellist, P. D.; Nicolosi, V. *Science* **2011**, *331*, 568.
(21) O'Neill, A.; Khan, U.; Coleman, J. N. *Chem. Mater.* **2012**, *24*, 2414.
(22) Nguyen, E. P.; Carey, B. J.; Daeneke, T.; Ou, J. Z.; Latham, K.; Zhuiykov, S.; Kalantar-zadeh, K. *Chem. Mater.* **2015**, *27*, 53.
(23) Hai, X.; Chang, K.; Pang, H.; Li, M.; Li, P.; Liu, H. M.; Shi, L.; Ye, J. H. *J. Am. Chem. Soc.* **2016**, *138*, 14962.
(24) Dong, L.; Lin, S.; Yang, L.; Zhang, J. J.; Yang, C.; Yang, D.; Lu, H. B. *Chem. Commun.* **2014**, *50*, 15936.
(25) Fan, X. B.; Xu, P. T.; Li, Y. C.; Zhou, D. K.; Sun, Y. F.; Nguyen, M. A. T.; Terrones, M.; Mallouk, T. E. *J. Am. Chem. Soc.* **2016**, *138*, 5143.
(26) Yao, Y. G.; Tolentino, L.; Yang, Z. Z.; Song, X. J.; Zhang, W.; Chen, Y. S.; Wong, C. P. *Adv. Funct. Mater.* **2013**, *23*, 3577.
(27) Gupta, A.; Arunachalam, V.; Vasudevan, S. *J. Phys. Chem. Lett.* **2015**, *6*, 739.
(28) Smith, R. J.; King, P. J.; Lotya, M.; Wirtz, C.; Khan, U.; De, S.; O'Neill, A.; Duesberg, G. S.; Grunlan, J. C.; Moriarty, G.; Chen, J.; Wang, J. Z.; Minett, A. I.; Nicolosi, V.; Coleman, J. N. *Adv. Mater.* **2011**, *23*, 3944.

(29) Zhang, W. T.; Wang, Y. R.; Zhang, D. H.; Yu, S. X.; Zhu, W. X.; Wang, J.; Zheng, F. Q.; Wang, S. X.; Wang, J. L. *Nanoscale* **2015**, *7*, 10210.

(30) Guan, G. J.; Zhang, S. Y.; Liu, S. H.; Cai, Y. Q.; Low, M.; Teng, C. P.; Phang, I. Y.; Cheng, Y.; Duei, K. L.; Srinivasan, B. M.; Zheng, Y. G.; Zhang, Y. W.; Han, M. Y. *J. Am. Chem. Soc.* **2015**, *137*, 6152.

(31) Liu, W. S.; Zhao, C. Y.; Zhou, R.; Zhou, D.; Liu, Z. L.; Lu, X. H. *Nanoscale* **2015**, *7*, 9919.

(32) Chou, S. S.; De, M.; Kim, J.; Byun, S.; Dykstra, C.; Yu, J.; Huang, J. X.; Dravid, V. P. *J. Am. Chem. Soc.* **2013**, *135*, 4584.

(33) Nguyen, E. P.; Carey, B. J.; Ou, J. Z.; van Embden, J.; Della Gaspera, E.; Chrimes, A. F.; Spencer, M. J. S.; Zhuiykov, S.; Kalantar-zadeh, K.; Daeneke, T. *Adv. Mater.* **2015**, *27*, 6225.

(34) Presolski, S.; Pumera, M. *Mater. Today* **2016**, *19*, 140.

(35) Paredes, J. I.; Munuera, J. M.; Villar-Rodil, S.; Guardia, L.; Ayan-Varela, M.; Pagan, A.; Aznar-Cervantes, S. D.; Cenis, J. L.; Martinez-Alonso, A.; Tascon, J. M. D. *ACS Appl. Mater. Interfaces* **2016**, *8*, 27974.

(36) Tuxen, A.; Kibsgaard, J.; Gobel, H.; Laegsgaard, E.; Topsoe, H.; Lauritsen, J. V.; Besenbacher, F. *ACS Nano* **2010**, *4*, 4677.

(37) Wang, T. Y.; Zhu, R. Z.; Zhuo, J. Q.; Zhu, Z. W.; Shao, Y. H.; Li, M. X. *Anal. Chem.* **2014**, *86*, 12064.

(38) Makarova, M.; Okawa, Y.; Aono, M. *J. Phys. Chem. C* **2012**, *116*, 22411.

(39) Kim, J. S.; Yoo, H. W.; Choi, H. O.; Jung, H. T. *Nano Lett.* **2014**, *14*, 5941.

(40) Ding, Q.; Czech, K. J.; Zhao, Y. Z.; Zhai, J. Y.; Hamers, R. J.; Wright, J. C.; Jin, S. *ACS Appl. Mater. Interfaces* **2017**, *9*, 12734.

(41) Chen, X.; Berner, N. C.; Backes, C.; Duesberg, G. S.; McDonald, A. R. *Angew. Chem., Int. Ed.* **2016**, *55*, 5803.

(42) Jeong, M.; Kim, S.; Ju, S. Y. *RSC Adv.* **2016**, *6*, 36248.

(43) De, M.; You, C. C.; Srivastava, S.; Rotello, V. M. *J. Am. Chem. Soc.* **2007**, *129*, 10747.

(44) Hong, R.; Fischer, N. O.; Verma, A.; Goodman, C. M.; Emrick, T.; Rotello, V. M. *J. Am. Chem. Soc.* **2004**, *126*, 739.

(45) Yee, C. K.; Jordan, R.; Ulman, A.; White, H.; King, A.; Rafailovich, M.; Sokolov, J. *Langmuir* **1999**, *15*, 3486.

(46) Li, X. N.; Robinson, S. M.; Gupta, A.; Saha, K.; Jiang, Z. W.; Moyano, D. F.; Sahar, A.; Riley, M. A.; Rotello, V. M. *ACS Nano* **2014**, *8*, 10682.

(47) Huo, S. D.; Jiang, Y.; Gupta, A.; Jiang, Z. W.; Landis, R. F.; Hou, S.; Liang, X. J.; Rotello, V. M. *ACS Nano* **2016**, *10*, 8732.

(48) Zheng, K. Y.; Setyawati, M. I.; Lim, T. P.; Leong, D. T.; Xie, J. P. *ACS Nano* **2016**, *10*, 7934.

(49) Hu, D. F.; Li, H.; Wang, B. L.; Ye, Z.; Lei, W. X.; Jia, F.; Jin, Q.; Ren, K. F.; Ji, J. *ACS Nano* **2017**, *11*, 9330.

(50) Zou, X. F.; Zhang, L.; Wang, Z. J.; Luo, Y. *J. Am. Chem. Soc.* **2016**, *138*, 2064.

(51) Sangsuwan, A.; Kawasaki, H.; Matsumura, Y.; Iwasaki, Y. *Bioconjugate Chem.* **2016**, *27*, 2527.

(52) Tripathy, A.; Sreedharan, S.; Bhaskarla, C.; Majumdar, S.; Peneti, S. K.; Nandi, D.; Sen, P. *Langmuir* **2017**, *33*, 12569.

(53) Pandit, S.; Karunakaran, S.; Boda, S. K.; Basu, B.; De, M. *ACS Appl. Mater. Interfaces* **2016**, *8*, 31567.

(54) Zhang, X.; Lai, Z. C.; Tan, C. L.; Zhang, H. *Angew. Chem., Int. Ed.* **2016**, *55*, 8816.

(55) Tang, Q.; Jiang, D. E. *Chem. Mater.* **2015**, *27*, 3743.

(56) Liu, T.; Wang, C.; Gu, X.; Gong, H.; Cheng, L.; Shi, X. Z.; Feng, L. Z.; Sun, B. Q.; Liu, Z. *Adv. Mater.* **2014**, *26*, 3433.

(57) Mak, K. F.; Lee, C.; Hone, J.; Shan, J.; Heinz, T. F. *Phys. Rev. Lett.* **2010**, *105*, 136805.

(58) Kozawa, D.; Kumar, R.; Carvalho, A.; Kumar Amara, K.; Zhao, W. J.; Wang, S. F.; Toh, M. L.; Ribeiro, R. M.; Castro Neto, A. H.; Matsuda, K.; Eda, G. *Nat. Commun.* **2014**, *5*, 4543.

(59) Chernikov, A.; Berkelbach, T. C.; Hill, H. M.; Rigosi, A.; Li, Y. L.; Aslan, O. B.; Reichman, D. R.; Hybertsen, M. S.; Heinz, T. F. *Phys. Rev. Lett.* **2014**, *113*, 076802.

(60) Nayak, A. P.; Pandey, T.; Voiry, D.; Liu, J.; Moran, S. T.; Sharma, A.; Tan, C.; Chen, C. H.; Li, L. J.; Chhowalla, M.; Lin, J. F.; Singh, A. K.; Akinwande, D. *Nano Lett.* **2015**, *15*, 346.

(61) Chen, Y. C.; Lu, A. Y.; Lu, P.; Yang, X. L.; Jiang, C. M.; Mariano, M.; Kaehr, B.; Lin, O.; Taylor, A.; Sharp, I. D.; Li, L. J.; Chou, S. S.; Tung, V. *Adv. Mater.* **2017**, *29*, DOI: 10.1002/adma.201770320

(62) Chou, S. S.; Sai, N.; Lu, P.; Coker, E. N.; Liu, S.; Artyushkova, K.; Luk, T. S.; Kaehr, B.; Brinker, C. J. *Nat. Commun.* **2015**, *6*, 8311.

(63) Yang, X.; Li, J.; Liang, T.; Ma, C. Y.; Zhang, Y. Y.; Chen, H. Z.; Hanagata, N.; Su, H. X.; Xu, M. S. *Nanoscale* **2014**, *6*, 10126.

(64) Boucher, H. W.; Talbot, G. H.; Bradley, J. S.; Edwards, J. E.; Gilbert, D.; Rice, L. B.; Scheld, M.; Spellberg, B.; Bartlett, J. *Clin. Infect. Dis.* **2009**, *48*, 1.

(65) Rasool, K.; Helal, M.; Ali, A.; Ren, C. E.; Gogotsi, Y.; Mahmoud, K. A. *ACS Nano* **2016**, *10*, 3674.

(66) Wang, Z. Y.; Zhu, W. P.; Qiu, Y.; Yi, X.; von dem Bussche, A.; Kane, A.; Gao, H. J.; Koski, K.; Hurt, R. *Chem. Soc. Rev.* **2016**, *45*, 1750.

(67) Singh, A. P.; Nicholls, P. *J. Biochem. Biophys. Methods* **1985**, *11*, 95.

(68) Basu, B. *Biomaterials science and tissue engineering: Principles and methods*; Cambridge University Press: 2017.